Pore fluid pressure and internal kinematics of gravitional laboratory air-particle flows: Insights into the emplacement dynamics of pyroclastic flows

Olivier Roche, S. Montserrat, Y. Niño, A. Tamburrino

Pore fluid pressure and internal kinematics of gravitational laboratory air-particle flows: Insights into the emplacement dynamics of pyroclastic flows

O. Roche,[1,2,3] S. Montserrat,[4] Y. Niño,[4] and A. Tamburrino[4]

Received 13 November 2009; revised 23 February 2010; accepted 16 April 2010; published 14 September 2010.

[1] The emplacement dynamics of pyroclastic flows were investigated through noninvasive measurements of the pore fluid pressure in laboratory air-particle flows generated from the release of fluidized and nonfluidized granular columns. Analyses of high-speed videos allowed for correlation of the pressure signal with the flow structure. The flows consisted of a sliding head that caused underpressure relative to the ambient, followed by a body that generated overpressure and at the base of which a deposit aggraded. For initially fluidized flows, overpressure in the body derived from advection of the pore pressure generated in the initial column and decreased by diffusion during propagation. Relatively slow diffusion caused the pore pressure in the thinner flow to be larger than lithostatic at early stages. Furthermore, partial auto-fluidization, revealed in initially nonfluidized flows, also occurred and contributed to maintain high pore pressure, whereas dilation or contraction of the air-particle mixture with associated drag and/or pore volume variation transiently led the pressure to decrease or increase, respectively. The combination of all these processes resulted in long-lived high pore fluid pressure in the body of the flows during most of their emplacement. In the case of the initially fluidized and slightly expanded (~3–4%) flows, (at least) ~70%–100% of the weight of the particles was supported by pore pressure, which is consistent with their inertial fluid-like behavior. Dense pyroclastic flows on subhorizontal slopes are expected to propagate as inertial fluidized gas-particle mixtures consisting of a sliding head, possibly entraining basement-derived clasts, and of a gradually depositing body.

Citation: Roche, O., S. Montserrat, Y. Niño, and A. Tamburrino (2010), Pore fluid pressure and internal kinematics of gravitational laboratory air-particle flows: Insights into the emplacement dynamics of pyroclastic flows, *J. Geophys. Res.*, *115*, B09206, doi:10.1029/2009JB007133.

1. Introduction

[2] Dense gravitational fluid-particle flows, for which interactions between the solid particles and the interstitial fluid (liquid or gas) may dominate the flow dynamics, commonly occur in the environment. Examples include debris flows, snow avalanches, and pyroclastic flows, for which the respective fluid phase is water, air, or (principally) volcanic gases [e.g., *Iverson*, 1997; *Hopfinger*, 1983; *Druitt*, 1998]. The present study deals with gas-particle flows, with a special emphasis on pyroclastic flows. These commonly occur during volcanic eruptions and result from the gravitational collapse of a lava dome or of an eruptive column, as well as from the sedimentation of a dilute ash cloud. They consist of a mixture of gas and particles that propagates downslope under the influence of gravity [e.g., *Druitt*, 1998; *Freundt and Bursik*, 1998; *Branney and Kokelaar*, 2002]. Possible additional sources of gas include release from the pyroclasts, burnt vegetation, and entrainment of the ambient air during emission at the vent and propagation. Pyroclastic flows are potentially highly destructive phenomena as they can propagate at speeds of several tens of meters per second, over distances of several tens of kilometers, even on slopes of only a few degrees. A better understanding of the fundamental mechanisms of these natural events, including modes of propagation and deposition, is crucial to better constrain numerical simulations in the context of hazard assessment.

[3] This paper is aimed at investigating the processes that act in natural two-phase gravity currents, and for this we report a series of pore fluid pressure measurements in laboratory air-particle flows. The concept of pore fluid pressure was developed in soil mechanics and has been used subsequently to investigate the dynamics of fluid-particle flows [see *Iverson*, 1997; *Major and Iverson*, 1999; *Major*, 2000; and references therein]. At the base of a static column (of

[1]Clermont Université, Université Blaise Pascal, Laboratoire Magmas et Volcans, Clermont-Ferrand, France.
[2]UMR 6524, LMV, CNRS, Clermont-Ferrand, France.
[3]IRD, R 163, LMV, Clermont-Ferrand, France.
[4]Department of Civil Engineering, Universidad de Chile, Santiago, Chile.

0148-0227/10/2009JB007133

height H) of solid particles with a lighter interstitial fluid (of density ρ_f), the hydrostatic pore fluid pressure is

$$P_h = \rho_f g H, \tag{1}$$

where g is the gravitational acceleration. If a vertical differential motion between the particles and the fluid occurs, so that the fluid and the particles move relatively upwards and downwards, respectively, viscous drag is generated and stresses are transmitted to the fluid phase. In consequence, a (so-called) dynamic pore fluid pressure arises, and the total pore pressure is then

$$P = P_h + P_s, \tag{2}$$

where P_s results from the buoyant weight of the solid particles counterbalanced by drag. If the weight of the particles is fully supported, then

$$P_s = (\rho_s - \rho_f)(1 - \varepsilon) g H, \tag{3}$$

where ρ_s is the particle density and ε is the interstitial pore volume fraction (voidage). The interparticle contact stresses, which vary as the inverse of the pore fluid pressure, then vanish as the granular column is fully fluidized. Hence, the value of the pore fluid pressure indicates the amount of the weight of the particles that is supported and gives insights into the degree of particle-particle interactions. Note that if the interstitial fluid is much less dense than the particles, as in the present study, the hydrostatic component of P in equation (2) is negligible, and when the granular column is fully fluidized

$$P \approx \rho_s (1 - \varepsilon) g H, \tag{4}$$

which corresponds to the "lithostatic" pressure in the column. Dynamic pore fluid pressure can be generated both when a vertical fluid flow is introduced to a static granular column (fluidization) and when a highly concentrated bed of particles settles in a static fluid (sedimentation). The latter case may occur in nature as a granular network contracts, thus generating high pore pressure and low interparticle contact stresses [*Major*, 2000], and this can be the cause of landslide initiation [*Hutchinson*, 1986; *Iverson et al.*, 1997; *Snieder and van den Beukel*, 2004; *Iverson*, 2005; *Montgomery et al.*, 2009]. In contrast, dilation of the granular network can generate a decrease of the pore pressure [*Iverson et al.*, 2000; *Okada et al.*, 2004; *Gabet and Mudd*, 2006]. Once pore pressure is generated, it may decrease through a diffusion process whose timescale is proportional to H^2/D, where H is then the characteristic drainage path length and D is the hydraulic diffusion coefficient [e.g., *Iverson*, 1997].

[4] Measurement of the pore pressure in fluid-particle gravitational flows has been performed in the field as well as in laboratory experiments. Data on natural flows are scarce, due to technical limitations and because these events are rare and hazardous. Pore pressure relative to the ambient of up to ~15 kPa was reported for debris flows and accounted for ~20% of the total normal stress [*Berti and Simoni*, 2005; *McArdell et al.*, 2007] whereas values of ~10–100 Pa were measured in snow avalanches [*Nishimura et al.*, 1995; *McElwaine and Turnbull*, 2005]. More investigations have been done on controlled laboratory experiments, during which excess pore pressure indicating partial support of the weight of the particles was commonly measured. Most experiments dealt with water-particle mixtures flowing on (inclined) channels aimed to simulate subaqueaous or subaerial flows, so that the flows propagated under either water [*Ilstad et al.*, 2004; *Cassar et al.*, 2005] or air [*Major and Iverson*, 1999; *Okura et al.*, 2002; *Okada and Ochiai*, 2008]. Only a few works have been carried out on air-particle flows. These include large scale flows of ping-pong balls on a ski jump [*McElwaine and Nishimura*, 2001] and laboratory scale experiments involving particles of polystyrene or snow [*Turnbull and McElwaine*, 2008, 2010].

[5] In the present study, we carried out measurements of the pore fluid pressure in dam break (i.e., transient) air-particles flows, generated from the release of an initially fluidized or nonfluidized granular column, that propagated on a horizontal substrate in the ambient atmosphere. This work was principally motivated by an earlier study, which showed that initially fluidized flows of fine particles under these conditions propagate as inertial currents of pure fluid for most their emplacement [*Roche et al.*, 2008]. This result suggested that the pore fluid pressure in the flows was long-lived and high enough to account for nearly complete fluidization. In order to test this hypothesis, we made detailed measurements of the spatial and temporal variation of the pore pressure in similar flows. The pressure data were then used, along with high-speed video analyses, to decipher the internal flow structure in terms of degree of fluidization and depositional processes.

2. Experimental Apparatus, Material, and Method

[6] We carried out dam break air-particle flow experiments in an apparatus consisting of a reservoir and a horizontal channel separated by a vertical sluice gate (Figure 1). The reservoir and the channel had a length of 20 cm and 300 cm, respectively, and both had a width of 10 cm. The particles in the reservoir were released into the channel as the gate was removed, and the flow generated then propagated until it came to halt and formed a deposit. The gate was lifted by means of a counterweight, thus ensuring rapid opening at consistent speed, and was connected to an electrical switch that indicated the moment of removal. In order to generate a fluidized column of particles in the reservoir, air was supplied by a compressor and pressure was reduced to 1 bar at the entrance of the device. Air was then dried and its volumetric flow rate controlled by a manometer. The flow entered into a windbox filled with coarse (few mm) particles in order to reduce the volume of air. It then passed through a 1 cm-thick porous plate with mean pore size of 20 μm, which allowed for uniform fluidization of the column of particles resting on the plate. The defluidization behavior of the static column in the reservoir with the gate closed was also investigated by using a manually-controlled solenoid valve that allowed for quasi-instantaneous (<20 ms) shut off of the air flux.

[7] Both the reservoir and the channel were equipped with pressure sensors located at various distances from the sluice gate, at one side of the reservoir at the lowermost position, and along the base of the channel. The pressure sensors, of piezoresistive type, were provided by ICSensors™ (model 154N). Their sensing package utilizes oil to transfer pressure

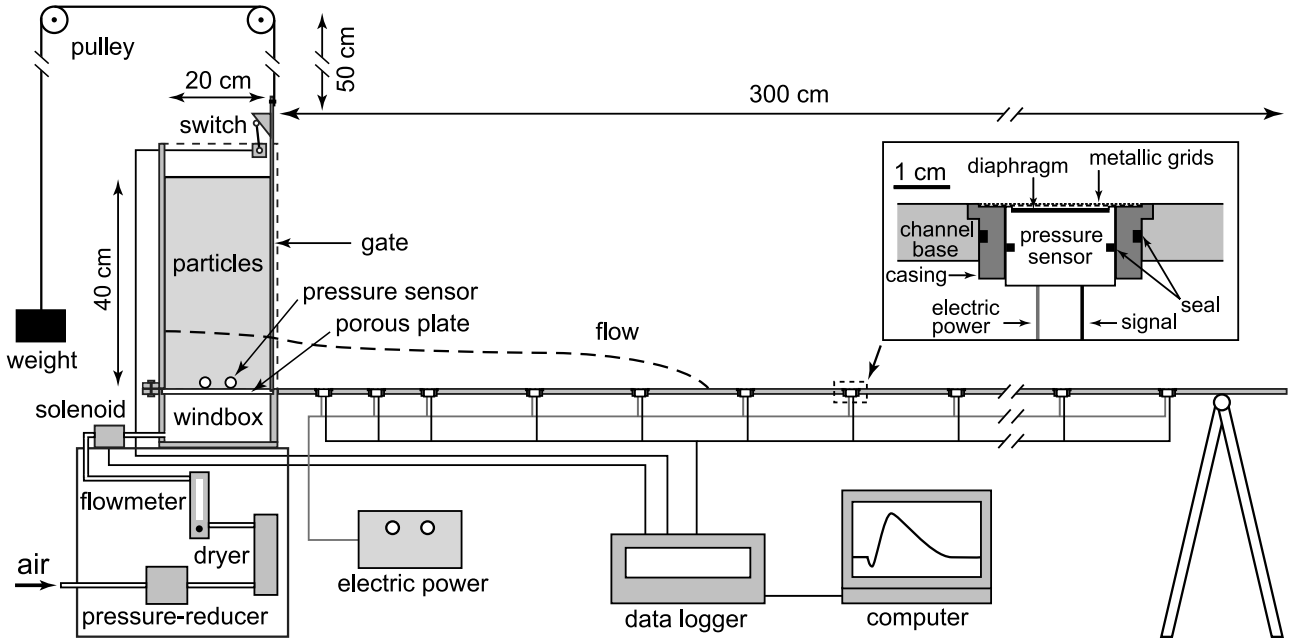

Figure 1. Experimental apparatus used in this study. Particles were placed in a reservoir, where they could be fluidized, and were released into a horizontal channel by means of a sluice gate. Sensors in the reservoir and in the channel, in horizontal and vertical position, respectively, allowed for noninvasive measurement of the pore fluid pressure. The close-up shows the casing in which the sensors were set, the distance between the diaphragm of the sensor and the grids being ~1 mm. See text for details.

from a stainless steel diaphragm to a sensing element having a frequency response of 1000 Hz. This element allows for the measurement of both positive and negative pressure relative to that of the ambient atmosphere. The sensors could measure pressure in the standard range of ~6.9 kPa (1 psi) in the channel or ~34.5 kPa (5 psi) in the reservoir with a typical noise of 5–10 Pa and 15–25 Pa, respectively. They were set in an aluminum casing specially designed for the experiments, which allowed for noninvasive measurement of the pore fluid pressure (see close-up in Figure 1). The diaphragm of the sensors was as close as possible to the air-particle mixture, both being separated by superposed metallic grids sealed on the casing. Two crossed thin grids of 38 μm-aperture (smaller than the particles used) were in contact with the mixture and were supported by a thicker grid of 600 μm-aperture that ensured rigidity of the assemblage. Electric power was supplied to the sensors, and when pressure was applied on the diaphragm the sensing element delivered a voltage of 0 to ±100 mV that was sent to a data logger that sampled at a frequency of 100–1000 Hz. Then, the signal was sent to a computer and was converted into pressure values through a linear calibration law. The solenoid valve and the gate switch were also connected to the data logger in order to indicate when the air supply was turned off during defluidization tests on static beds and when the gate was lifted in dam break flow experiments, respectively.

[8] The particles used were the same as those in a previous study on dam break granular flows by *Roche et al.* [2008], and were spherical glass beads of grain size range 60–90 μm (with a mean of 75 μm) and density ρ_s~2500 kg m^{-3}. The bulk density of the loosely packed granular column was $\rho_b \sim \rho_s(1-\varepsilon) = 1450 \pm 50$ kg m^{-3}, thus indicating a pore volume fraction $\varepsilon \sim 0.42 \pm 0.02$. Concerning the fluidization processes when air was introduced vertically at the base of the column in the reservoir, the particles belonged to the group A as classified by *Geldart* [1973] [see also *Rhodes*, 1998]. For this type of particles, homogeneous expansion occurs over a range of air mean velocity, equivalent to the mean volumetric flow rate divided by the cross sectional area of the granular bed, between the minimum fluidization velocity (U_{mf}) and the minimum bubbling velocity ($U_{mb} > U_{mf}$). At U_{mf}, the bed is nearly fully supported as its weight is counterbalanced by the drag force generated by the interstitial air flow. In consequence, the pore fluid pressure approaches the maximum value given by equation (4). Expansion of the granular network occurs at higher air velocity and is maximum at U_{mb}, above which air bubbles form. It is important to note that ash-rich matrices of pyroclastic flow deposits have a typical group-A behavior when fluidized [*Druitt et al.*, 2007], and the use of such type of particles in our experiments ensures the basis for dynamic similarity with the natural system. In complementary experiments, we used larger particles as markers at low volume fraction (<10%) to visualize the internal flow kinematics, and these were either 700 μm-glass beads of density equal to ρ_s or 1–2 mm-plastic particles of density close to ρ_b.

[9] Most flows were generated from the release of fluidized or dry (i.e., nonfluidized) granular columns having an initial loosely-packed height $h_0 = 40$ cm. We also performed complementary experiments at $h_0 = 10$–30 cm. For fluidized columns, experiments were carried out at $U_{mf} = 0.82$ cm s^{-1} and $U_{mb} = 1.28$–1.36 cm s^{-1}, at which the bulk expansion was nil and ~3–4%, respectively, and in both cases the initial pore fluid pressure was then $P \sim \rho_s(1-\varepsilon)gh_0$ (i.e., equation (4)). We began acquisition of the pressure data in

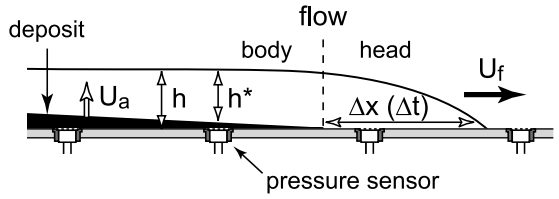

Figure 2. Structure of the flows in the channel (the vertical scale is exaggerated). The basal deposit (black) in the flow body forms behind the sliding head at a distance Δx (and time interval Δt) from the front that propagates at velocity U_f, and aggrades at a rate U_a. At a given location in the body, the height of the mobile part overlying the deposit (h^*), smaller than the total flow height (h), decreases with time.

the reservoir and in the channel before gate opening. The flows were recorded in their entire length with a high-speed video camera through the lateral transparent side walls of the apparatus, at a rate of 100–250 frames per second. The videos were subsequently analyzed to determine the flow front kinematics and the flow height above the sensors as a function of time. When investigating the internal flow kinematics, we considered a much smaller zone typically of length 10–30 cm. Such close-up views were necessary in order to accurately capture the motion of the marker particles.

3. Results

3.1. General Flow Behavior

[10] The kinematics of dam break granular flows was studied in detail by *Roche et al.* [2008]. The fundamental issues of their investigation are reported here because they

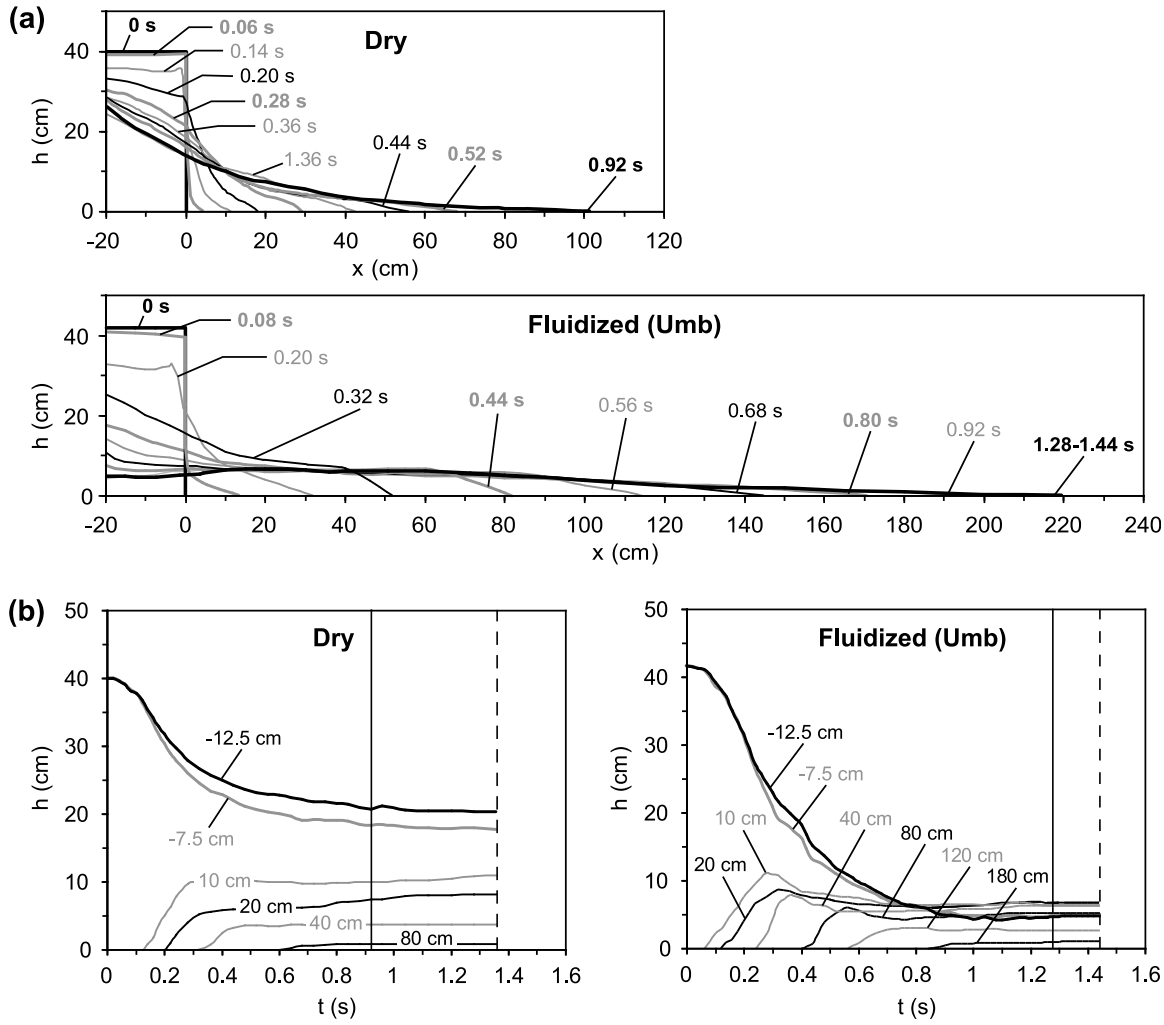

Figure 3. (a) Surface flow profiles as a function of time after release (see labels), for dry and initially fluidized (at U_{mb}) flows. The reservoir gate is at distance $x = 0$. Thick black lines represent the initial column in the reservoir (at 0 s) and the profile when the flow front stops, the latter being at 0.92 s (dry) and 1.28 s (U_{mb}). Note that superficial motion occurs until 1.36 s (dry) and 1.44 s (U_{mb}). (b) Total flow height (h) as a function of time (t) after gate opening, extracted from the surface flow profiles in Figure 3a. Labels denote the distance from the reservoir gate. The vertical plain and dashed lines indicate the time at which the flow front stops and superficial motion ceases, respectively.

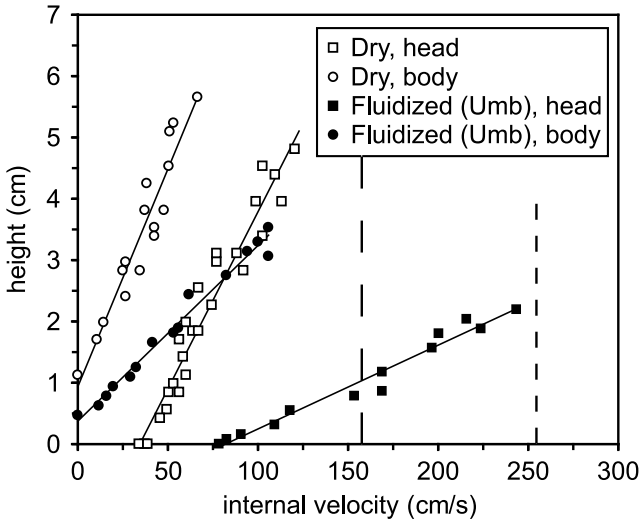

Figure 4. Internal horizontal velocity of the markers in the flows as a function of height. Measurements were made at a distance from the reservoir gate of one third and one half of the flow run out in dry and initially fluidized flows, respectively, approximately at half the length of the flow head and body, and during time intervals of ~0.02–0.04 s. Linear fits are assumed for simplicity. Nonzero height at zero internal velocity in the flow body corresponds to the top of the basal deposit. Vertical lines denote the flow front velocity in dry (large-dashed) and initially fluidized (small-dashed) flows. The shear rate in the initially fluidized flow is ~74 s^{-1} (head) and ~35 s^{-1} (body), and in the dry flow is ~14–18 s^{-1}.

will be referred to hereafter to discuss the results of the present study. Flows resulting from the release of granular columns of initial height h_0 and with a height-to-length ratio up to 3 propagated in three distinct phases, according to the kinematics of their front (see snapshots in Figure 4 of *Roche et al.* [2008]). The distance and time at which transition between the phases occurred depended on the length scale h_0 and on the time scale $(h_0/g)^{1/2}$, respectively, the latter being proportional to the time scale of the column free fall. The flows first steadily accelerated or had a nearly constant (small) velocity as the column collapsed, before they entered into a second, constant (high) velocity phase. They then decelerated and stopped during a third (stopping) phase. For initially fluidized flows, the transition between the second and the third phase occurred when the difference in height between the collapsing column in the reservoir and the flow in the channel, thus generating a pressure gradient, had become negligible. An important observation was that granular flows generated from the collapse of slightly expanded (2.5–4.5%) columns fluidized at U_{mb} behaved as inertial flows of water as their front velocity was close to that observed for such flows, $U_f \sim (2gh_0)^{1/2}$, until the beginning of the stopping phase, which occurred at ~65% and ~80% of the flow duration and runout, respectively.

[11] In the present study, repetition of the experiments at h_0 = 40 cm showed good reproducibility, with runout (duration) of 102±2 cm (0.90±0.03 s), 187±3 cm (1.12±0.04 s), and 221±4 cm (1.28±0.04 s) for flows of dry material and those generated from columns fluidized at U_{mf} and U_{mb}, respectively. Most characteristics of flows with initial fluidization at U_{mf} were similar to those at U_{mb}, though flow duration and run out were a bit smaller, and because of that are not always presented in detail hereafter. The experiments carried out with markers revealed a basal deposit that formed behind a sliding head (where no deposition occurred), and whose upper surface aggraded upwards with time in the flow body (Figure 2). In consequence, the height of the overlying mobile part at a given location in the body decreased with time as the flow propagated into the channel, and the basal deposit took the form of a slender wedge. In the following sections, we report the characteristics of the flows and of their basal deposit, and then use the results to analyze and discuss the pore fluid pressure data.

3.2. Characteristics of the Flows and of Their Basal Deposit

[12] Surface flow profiles were acquired from the video images (see Movies S1 and S2)[1] and are shown in Figure 3a. In dry flows, the profiles are wedge shaped, with the height decreasing downstream at a given time, and the surface slope is relatively steep except at the front. In contrast, initially fluidized flows spread much more as most of the material is evacuated from the reservoir. This leads to nearly flat profiles at late stages with a maximum height at the entrance of the channel. We note that for both types of flows some superficial motion occurs after the flow front has stopped. The distal limit of this motion migrates upstream and then stops at the rear of the reservoir or at the entrance of the channel in case of dry or initially fluidized flows, respectively. In dry flows, late avalanches result in a slight increase and decrease of the total flow height at the entrance of the channel and in the reservoir, respectively. In the reservoir, the surface slope then approaches the angle of repose of the material (~28°). In contrast, late superficial motion in initially fluidized flows does not modify the surface flow profile significantly. Figure 3b shows the total flow height as a function of time (h, in Figure 2) extracted from the surface flow profiles. The height in the reservoir decreases with time and remains larger or becomes smaller than that in the channel in case of dry and initially fluidized flows, respectively. In dry flows, the total height at a given location in the channel increases rapidly (in ~0.10–0.15 s) and remains thereafter approximately constant with time, though it increases slightly close to the reservoir gate because of late superficial avalanches. In contrast, in initially fluidized flows, the flow height rapidly increases to a maximum (in ~0.15–0.20 s), then decreases and finally slightly increases at late stages.

[13] The internal velocity field of the flows was investigated from high-speed videos of the experiments involving markers. The trajectory of these markers was principally in the horizontal direction, except close to the reservoir in the upper portion of the flows and at the flow front. Figure 4 shows that both the flow head and body are pervasively sheared as the internal velocity increases upwards. We highlight that the lowermost part of the head slides over the channel base, whereas in the upper parts the internal velocity approaches the flow front velocity, such suggesting that drag and air entrainment on the upper free surface are negligible. In the body, the velocity is zero at the top of the

[1] Animations are available in the HTML.

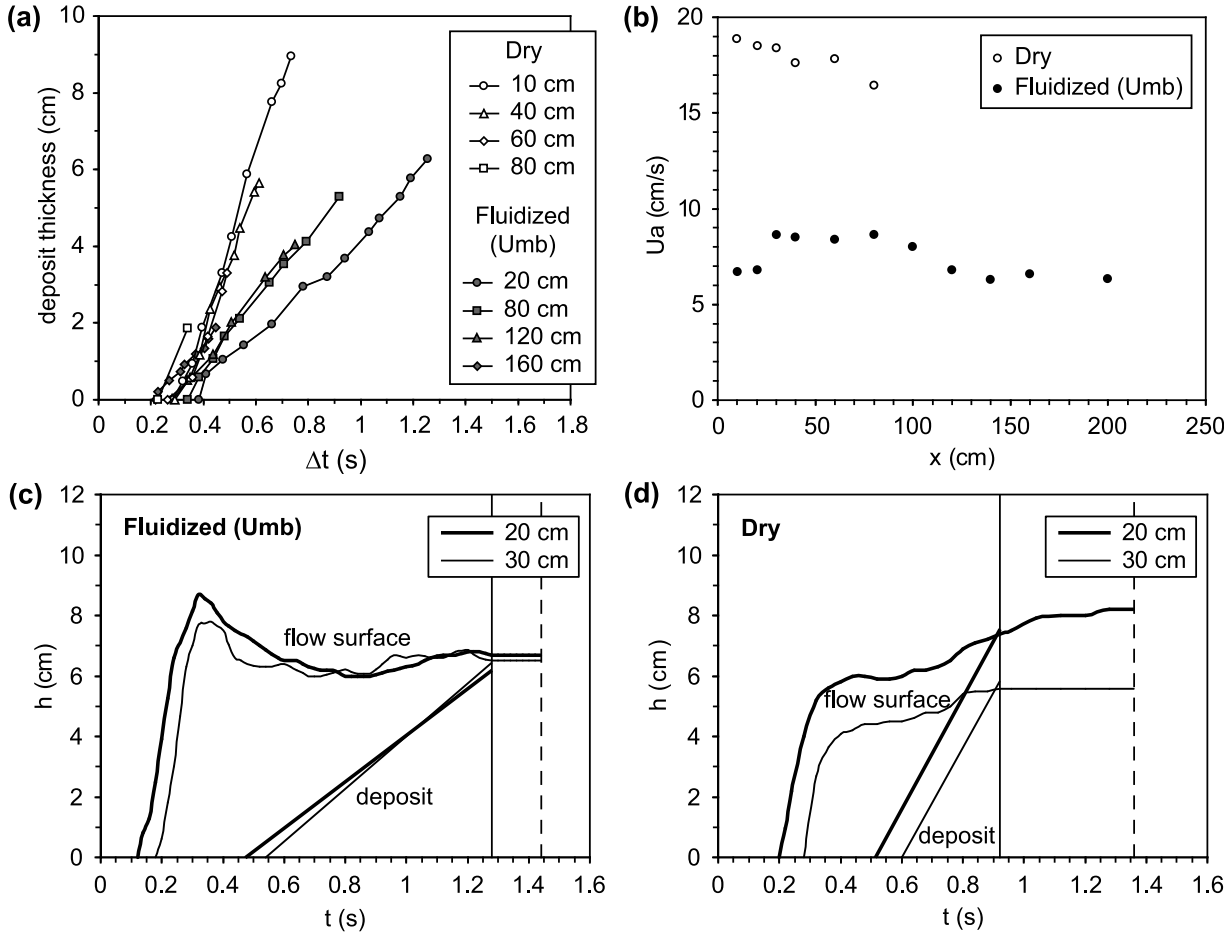

Figure 5. Characteristics of the basal deposits in dry and initially fluidized (at U_{mb}) flows. (a) Thickness of the basal deposit as a function of time, at various distances from the reservoir gate in the channel, where $\Delta t = 0$ corresponds to the arrival of the flow front. Measurements were made at other locations but are not shown for clarity. (b) Mean aggradation velocity (U_a) of the basal deposit as a function of the distance from the reservoir gate (x), according to linear fit of the data in Figure 5a. In Figures 5a and 5b error bars have about the size of the symbols and are not shown. (c and d) Observed total flow height (flow surface) taken from Figure 3, and calculated thickness of the deposit (h_d) as a function of time (gate opening at $t = 0$) assuming $h_d = U_a t$, at 20 and 30 cm from the reservoir gate. The vertical solid and dashed lines indicate when the flow front stops and superficial motion ceases, respectively.

basal deposit, and then increases upwards to a value significantly smaller than that of the front velocity. Note that velocities in the flow head higher than that in the body imply that the flows stretch during propagation. The shear rate in initially fluidized flows is smaller in the body than in the head, whereas it is approximately the same in both regions in dry flows. Although the shear rate just above the channel base and the top of the basal deposit might be larger [e.g., *Girolami et al.*, 2010], this could not be detected with the method we used. For initially fluidized flows, particles at the front came from the lower part of the initial column. A weak caterpillar effect was evidenced at late stages of emplacement, with particles at the front overran by those located behind them and then incorporated into the basal part of the sliding head.

[14] The characteristics of the basal deposits were investigated in detail in flows with markers (Figure 5). The video camera was located at various distances from the reservoir gate in the channel, and recordings were obtained by repeating the experiments, as permitted by their high reproducibility. We measured the thickness of the basal deposit, assuming that this corresponded to the distance between the channel base and the markers when their motion ceased. Figure 5a shows that the deposit aggradation begins ~0.2–0.3 s and ~0.2–0.4 s after the passage of the front in dry and initially fluidized flows, respectively, and that this time interval (Δt_{dep}) tends to decrease as the distance from the reservoir gate increases (see detailed data in Figure 7). The deposit thickness increases almost linearly with time, so that the aggradation velocity (U_a) can be determined by simply assuming a linear fit of the data. Figure 5b reveals that U_a is larger in dry flows than in initially fluidized ones, and varies slightly as the distance in the channel increases. In fact, U_a decreases from ~19 to ~16.5 cm s^{-1} in dry flows, whereas it first increases from ~6.5 to ~8.5 cm s^{-1} and then decreases to ~6.5 cm s^{-1} in initially fluidized ones. The thickness of the

deposit (h_d) as a function of time (t) was then calculated from the observed onset of aggradation by assuming $h_d = U_a t$. Figures 5c and 5d show that h_d calculated is about equal to the measured total flow thickness when the flow front stops.

3.3. Pore Fluid Pressure in the Flows

[15] The pore fluid pressure data are presented in Figure 6. It is important to bear in mind that measurements were made relative to the ambient, at which $P = 0$. Hence the terms underpressure or overpressure used hereafter means that the pressure is less or more than the atmospheric pressure, respectively. We report the pore pressure measured by the sensors, P, as well as the normalized pressure P/P_L and P/P_L*, with lithostatic terms P_L and P_L* defined as

$$P_L = \rho g h \tag{5}$$

and

$$P_L^* = \rho g h^*, \tag{6}$$

where ρ is the bulk density of the flow assumed to be equal to that of the initial column (ρ_b~1450 kg m^{-3}), h is the total flow height extracted from the surface flow profiles in Figure 3, and $h^* = h - h_d$ where $h_d = U_a t$ is the calculated thickness of the basal deposit taking into account the time interval Δt_{dep} between the passage of the front and the onset of deposition (i.e., Figure 5). Regarding equation (6), we assume that the pressure increases from the flow surface to a maximum value at the top of the deposit and is then constant down to the base of the channel. Note that for fluidized columns in the reservoir $P_L^* = P_L$. For a few sensors, U_a and Δt_{dep} could not be determined accurately because of a lack of markers on the videos. In that case, we assumed a simple linear interpolation between values of these parameters measured at adjacent locations. Calculation of P_L* was stopped as P/P_L* (1) became negative as $h^* < 0$ or (2) increased abruptly to very high values (~5–10) as h* approached h because of the uncertainty in the measurement of h and on the estimate of h*. We also report the flow front position in order to discuss the pore fluid pressure data in link with the phases of flow emplacement described in Section 3.1. As discussed below, the correlation between those phases and the pressure signals is good in most cases.

[16] For initially fluidized flows, the pore fluid pressure in the reservoir before gate opening (P~5500 Pa) indicates that nearly full bed support is achieved at U_{mb} (P/P_L~1) whereas ~90% of the weight is supported at U_{mf} (P/P_L~0.9) (Figure 6). Once the gate is lifted and the material enters into the channel, P rapidly drops to ~1000 Pa. Pressure then oscillates while increasing up to ~4500 Pa at the end of the first, collapse phase, and this maximum pressure is more than lithostatic as P/P_L~1.5. The ratio P/P_L then varies a bit until the beginning of the stopping phase, and then returns to ~0.9–1 when the flow front stops as the air flux still fluidizes the particles remained in the reservoir. At that stage, P at U_{mf} is larger than that at U_{mb} because the bed height is higher as less particles were evacuated from the reservoir, and waves at the surface of the fluidized bed then cause pressure oscillation in both cases. In the channel, the sensors reveal all the same pressure signal pattern (Figure 7a). Deviation from atmospheric pressure is recorded as soon as the flow front arrives at the sensors, as confirmed by close examination of the videos and the front kinematic data in Figure 6. The pressure signal first reveals a negative, almost symmetrical stage (relative to the minimum value), followed by a positive, asymmetrical stage as the pressure rapidly increases to a maximum value and then slowly decreases. The duration of the underpressure stage increases at increasing distance from the gate, and the minimum pressure ($P_{\min}$) is down to ~ −500 to −600 Pa and is correlated at a first order to the flow front velocity, U_f. We note that during the first phase of emplacement for h_0 = 40 cm (as in Figure 6), $P_{\min}$ varies while U_f is nearly constant. However, complementary experiments at lower h_0, for which U_f steadily increased during this first phase, showed that $P_{\min}$ was proportional to U_f. Positive pressure values for flows initially fluidized at U_{mf} are close to that of those fluidized at U_{mb} for sensors located up to 20 cm from the gate, and then are significantly smaller beyond. The maximum pressure ($P_{\max}$) is less than that in the reservoir at the same time, and it decreases with distance. However, the pore pressure can be more than lithostatic close to the gate (at 5 to 20 cm) during the constant velocity phase as maximum P/P_L is larger than 1, and is similar to that (P/P_L~1.5, at U_{mf}) or larger than (P/P_L~2, at U_{mb}) in the reservoir. P/P_L* is larger than P/P_L at a given time after the onset of deposit aggradation, because $h^* < h$, and remains high for most the sensors. An important result is that high pore pressure is maintained approximately until the beginning of the stopping phase. For instance in flows initially fluidized at U_{mb}, up to ~90%, ~75%, and ~65% of the weight of the flow overlying the basal deposit is supported at distances of 30, 40, and 60 cm, respectively. We highlight (1) that at the moment of maximum pore pressure, the flow front is located much further away in the channel than the corresponding sensor, that is at ~110 cm (sensor at 30 cm), ~130 cm (40 cm), and ~165 cm (60 cm), and (2) that the amount of weight supported would be even larger in case the bulk flow density would be smaller than that assumed (ρ_b~1450 kg m^{-3}) because of dilation of the air-particle mixture. Note that at a

Figure 6. Pore fluid pressure in initially fluidized ((left) at U_{mb}, and (middle) U_{mf}) and (right) dry flows (note that the vertical scales are different), generated from columns of loosely-packed height h_0 = 40 cm. The graphs show the measured pore pressure (P) where $P = 0$ corresponds to (a–c) the atmospheric pressure, and the ratios (d–f) P/P_L and (g–i) P/P_L* as a function of time, $t = 0$ indicating gate opening (small-dashed vertical line). Only positive pressure is considered for P/P_L and P/P_L*. The location of the sensors is relative to the reservoir gate, so that values are negative in the reservoir and positive in the channel. Solid and large-dashed vertical lines indicate when the flow front stops and superficial motion ceases, respectively. Numbers in circle denote the collapse (1), constant velocity (2), and stopping (3) phases of flow emplacement, based on the kinematics of the front whose position (x) is reported (thick black curve, right scale), and their relative duration is indicated by small vertical dashed lines.

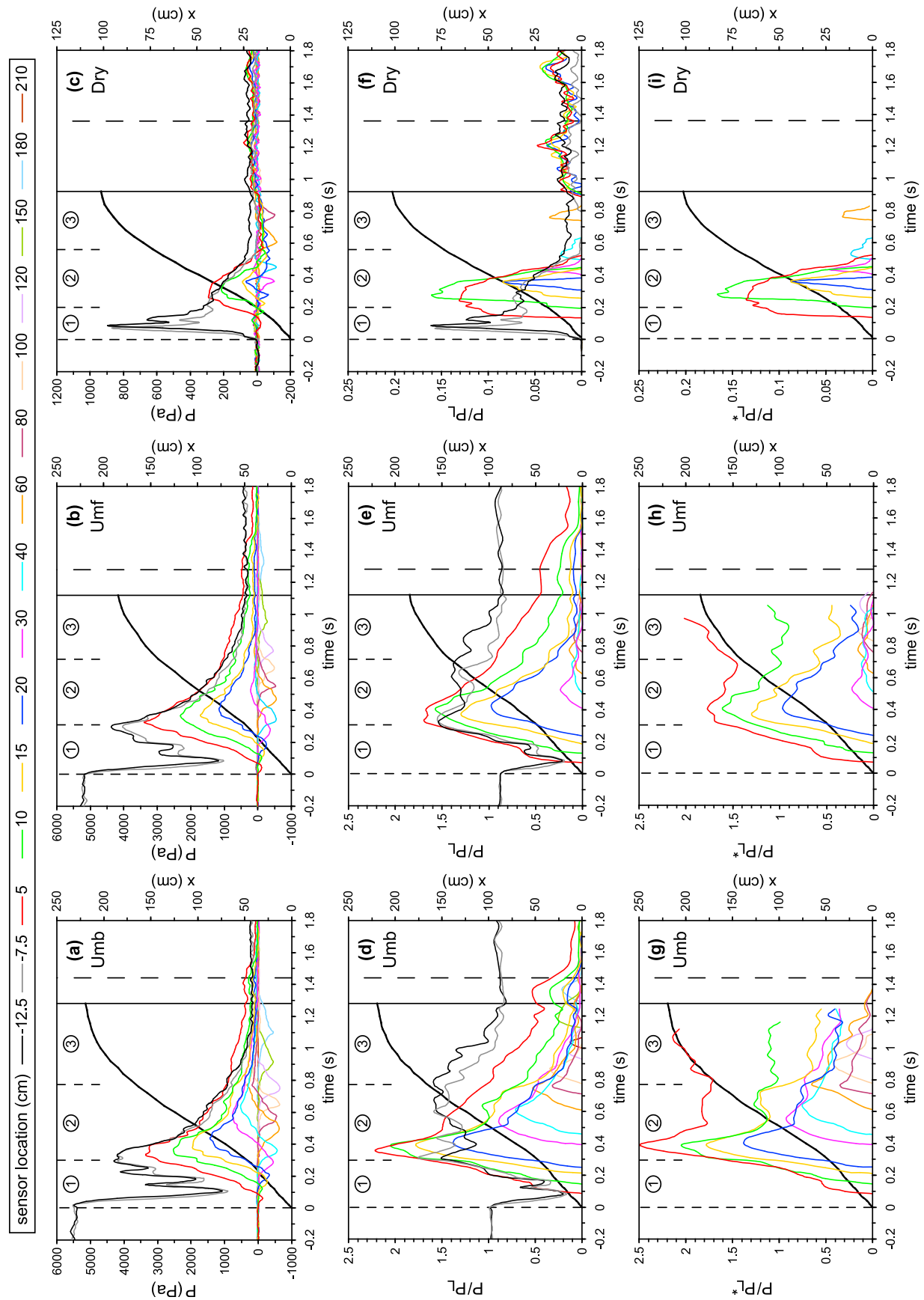
sensor location (cm)
-12.5
-7.5
5
10
15
20
30
40
60
80
100
120
150
180
210
(a) Umb
(b) Umf
(c) Dry
(d) Umb
(e) Umf
(f) Dry
(g) Umb
(h) Umf
(i) Dry
P (Pa)
P/PL
P/PL*
x (cm)
time (s)
① ② ③

Figure 6

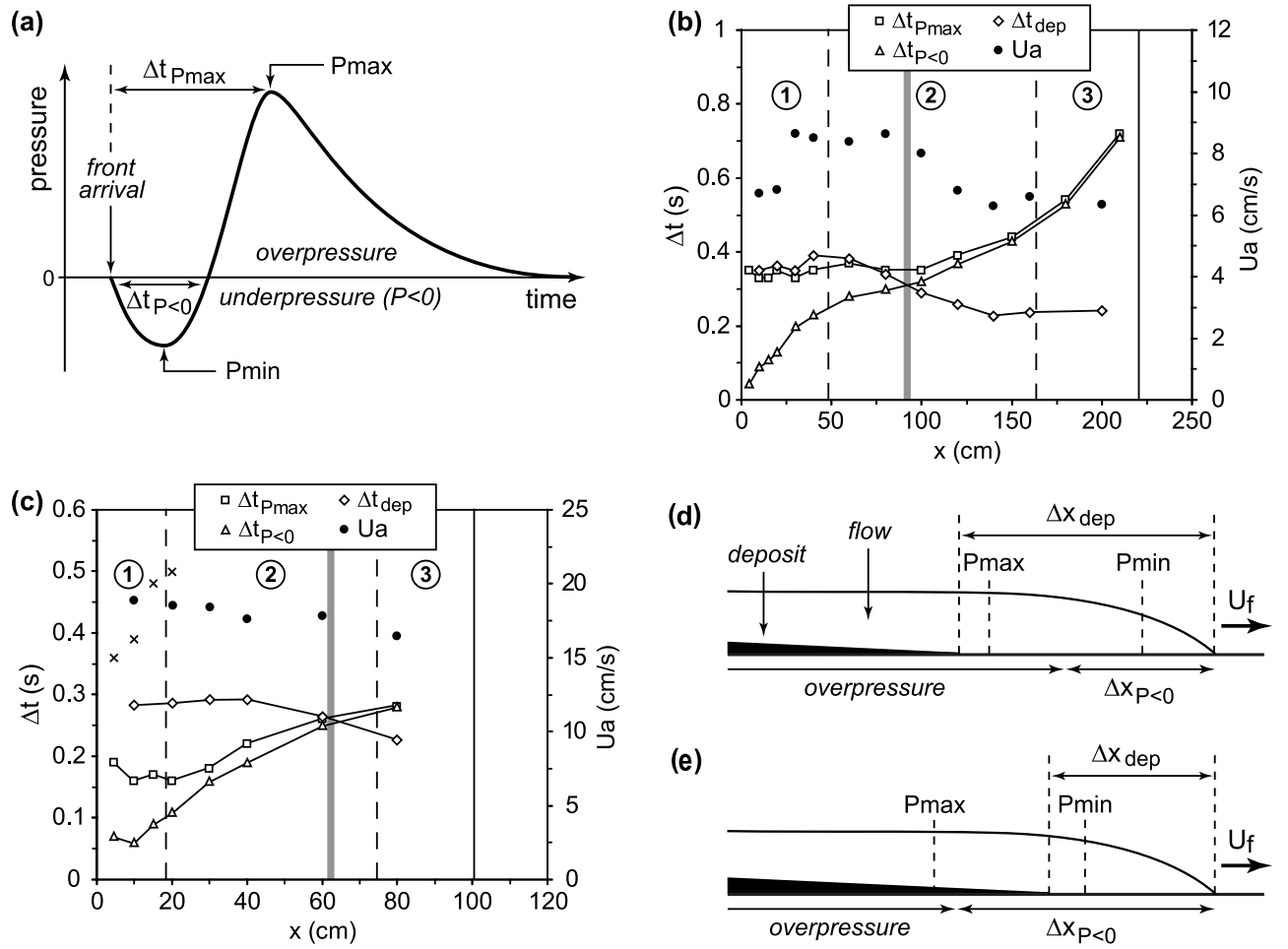

Figure 7. Characteristics of the pore fluid pressure data and of the basal deposits. (a) Typical pressure signal in the channel, showing successive stages of underpressure and overpressure. Zero pressure corresponds to atmospheric. Variation as a function of the distance from the reservoir gate (x) of the duration of the underpressure stage ($\Delta t_{P<0}$), and of the time interval between the front arrival and the maximum pressure (Δt_{Pmax}) or the onset of deposit aggradation (Δt_{dep}), for (b) initially fluidized (at U_{mb}) and (c) dry flows. In Figure 7c, crosses indicate the duration of the second underpressure stage (see text for details). The deposit aggradation velocity (U_a) taken from Figure 5 is also shown (right scale). Numbers in circle denote the collapse (1), constant velocity (2), and stopping (3) phases of flow emplacement whose corresponding length is delimited by vertical dashed lines. The vertical solid line indicates the flow run out. Interpretation of the internal flow structure from Figures 7b and 7c, when the flow front is at a distance (d) shorter or (e) longer than that indicated by the grey bar in Figures 7b and 7c. Horizontal arrows indicate corresponding lengths assuming $\Delta x = U_f \Delta t$, and vertical dashed lines show the location of P_{min} and P_{max}. Note that the underpressure zone can extend within that of the basal deposit (Figure 7e), but P_{min} is still ahead the deposit.

given time, the flows have a longitudinal pressure gradient as P/P_L* decreases with distance from the reservoir (Figure 8). When the flows decelerate during their stopping phase, P/P_L* decreases but the most distal sensors indicate that up to 25–40% (at U_{mb}) and 15–20% (at U_{mf}) of the weight of the particles is still supported. Pressure returns to atmospheric at the end of flow propagation, except for the most proximal sensor (at 5 cm), as air flowing from the reservoir is diverted sideways, so that the final deposit is still partially fluidized. Note that a slight pressure increase occurs for sensors close to the gate (5–20 cm) after the flow front has stopped due to late-stage superficial flow, and that very small amount of pressure is still present shortly after motion has totally ceased.

[17] Interestingly, pore fluid pressure is also detected in initially dry flows, though it is much smaller than in initially fluidized ones. In the reservoir, P increases rapidly up to ~850 Pa during the collapse phase as most the material above the sensors is in motion, showing that at least ~16% of the weight of the column is supported. The pressure then steadily decreases, though some slight fluctuation occurs after the peak value. Very small residual pressure corresponding to only ~1–2% of the weight of the collapsed column is measured at the latest stages and even after motion has completely ceased. In the channel, the pressure

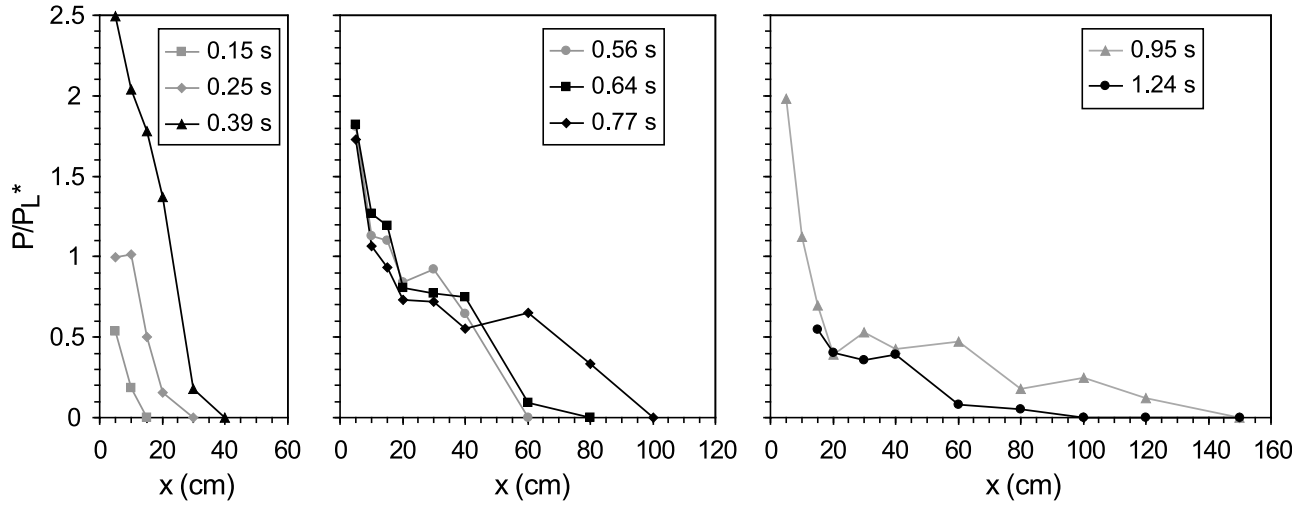

Figure 8. Lateral pressure gradient at different times after release in the initially fluidized (at U_{mb}) flow whose data are presented in detail in Figure 6. The pressure ratio P/P_L* decreases as the distance in the channel (x) increases. Note that pressure is more than lithostatic (P/P_L*>1) at early stages and/or close to the reservoir gate (at x = 0).

signal has the same characteristics as for initially fluidized flows, though it is weaker, as it reveals successive underpressure and overpressure stages. $P_{\min}$ decreases as the flow front velocity increases during the collapse phase, and $P_{\max}$ decreases with the distance from the gate. Values of P/P_L similar to that in the reservoir at early stages (~0.13–0.16) are measured at the entrance of the channel (at 5–10 cm) at the beginning of the constant velocity phase. We note that close to the gate (at 5–20 cm), (1) overpressure may be followed by a second underpressure stage that appears approximately at the onset of basal deposition and whose minimum value is close to that of the first one and (2) that some very small residual pore pressure similar to that in the reservoir is measured after the flow has stopped.

[18] The detailed characteristics of the pressure signals are reported in Figure 7. They reveal variations similar to that of the deposits at increasing distance from the reservoir gate, and a transition occurs during the constant velocity phase. Before the transition (grey bar in Figures 7b and 7c), the time interval between the front arrival and (1) the maximum overpressure (Δt_{Pmax}) or (2) the onset of deposit aggradation (Δt_{dep}) varies slightly and is larger than the duration of the underpressure stage ($\Delta t_{P<0}$), which increases almost steadily. Transition occurs when these time intervals are almost equal to $\Delta t_{P<0}$, whose rate of change then decreases. Beyond the transition, for initially fluidized flows, $\Delta t_{Pmax} \sim \Delta t_{P<0}$ and both increase, whereas Δt_{dep} varies similarly to the deposit aggradation velocity as it decreases slightly with distance. At that stage, evolution of the time intervals in dry flows is less clear. These results imply that the basal deposit begins to aggrade behind both the location of $P_{\max}$ and the zone of underpressure at early stages of propagation (Figure 7d), whereas it aggrades ahead of $P_{\max}$ and within the underpressure zone at later stages (Figure 7e). Note that the length of the sliding head does not vary much until the stopping phase. This shows that the tip of the basal deposit migrates downstream, as the particles sediment from the flow body, at a velocity close to that of the flow front.

3.4. Comparison With Defluidization of Static Beds

[19] Initially fluidized flows basically defluidize while they propagate in the channel. In order to investigate the defluidization processes, we performed experiments on static columns in the reservoir with the gate closed and made comparison of their defluidization timescale with that of the flows. The aim of these tests was to assess if the flows deaerate accordingly to the simple configuration of a static column or if other processes may act. Experiments consisted of columns of various heights fluidized at U_{mf} and U_{mb}, then the air supply was turned off instantaneously using the solenoid valve and the pressure was recorded by the sensors in the reservoir. At U_{mb}, this corresponded to a bed collapse test [*Geldart and Wong*, 1985; *Druitt et al.*, 2007].

[20] Comparison of the flows and the static columns defluidization timescales is not straightforward for the following reasons. (1) The flow height varies spatially and temporarily whereas columns in the reservoir have a constant height (neglecting the small initial expansion at U_{mb}). For simplicity, we have considered the nearly constant flow height (h~6 cm) observed during the dominant constant velocity phase (see Figure 3) and we made comparisons with experiments on static columns of similar heights. (2) The pore fluid pressure in the flows can be more than lithostatic close to the reservoir (see Figure 6). (3) The weight of a fluidized static column is not entirely supported at small height typically <20 cm, possibly because of heterogeneities caused by air flow channeling [*Gilbertson et al.*, 2008]. In consequence, the initial normalized pore pressure for the small static columns investigated was less than for the 40 cm-high columns used to generate the flows. (4) Deposit aggradation occurs in the flows, but not in static columns initially fluidized at U_{mf} because of the negligible expansion of these columns; furthermore, onset of aggradation in the flows occurs after a significant time interval following the passage of the front, whereas a deposit forms immediately in static columns fluidized at U_{mb} once air flux is no longer supplied.

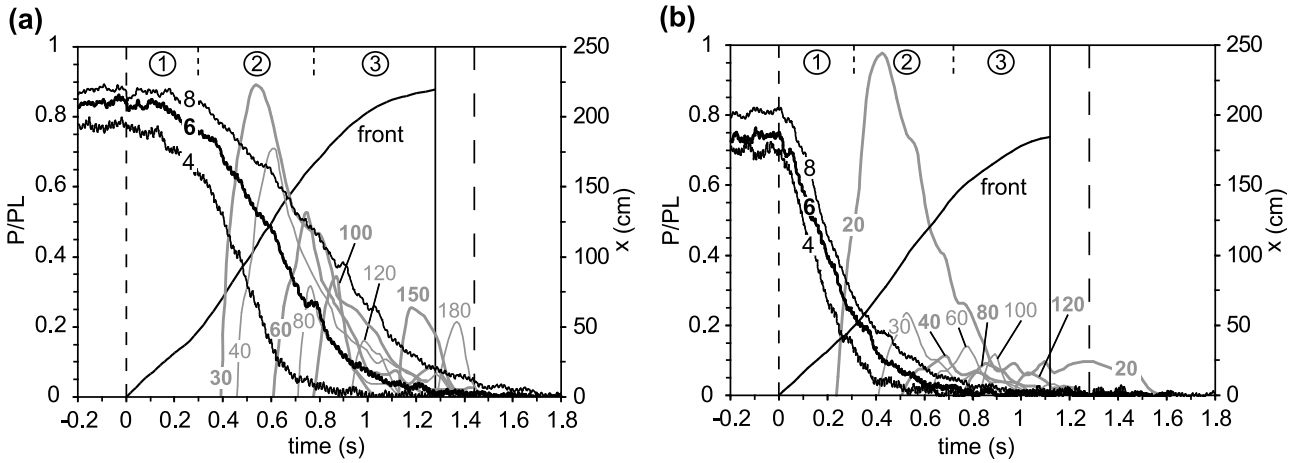

Figure 9. P/P_L as a function of time for granular columns initially fluidized at (a) U_{mb} or (b) U_{mf}, for static columns in defluidization tests (black) and for flows (grey, data from Figure 6 at $P/P_L < 1$). Indices denote the height of the loosely packed static columns (black, in cm) and the sensor location in the channel for flow experiments (grey, in cm). The flow front position is also shown (x, right scale), and numbers in circle denote the collapse (1), constant velocity (2), and stopping (3) phases of flow emplacement whose duration is indicated by small vertical dashed lines. The vertical solid lines point out when the flow front stops, and vertical dashed lines designate the moment the solenoid valve is turned off (static beds) or the reservoir gate is open (flows) at $t = 0$ and when superficial flow motion ceases at late stages. Measurements for static columns were made with sensors measuring pressure in the range of ~34.5 kPa (5 psi) and at high sampling frequency (600–800 Hz), thus explaining the noisy aspect of the curves.

[21] Figure 9 shows P/P_L as a function of time in defluidizing static columns, and the data are compared to that of the flows taken from Figure 6. Results are reported for a range of column height H = 4–8 cm including the nearly constant flow height (~6 cm) observed during the dominant constant velocity phase. As mentioned above, P/P_L for small static columns before the air supply is turned off decreases as the column height decreases and it is equal to ~0.78–0.88 at U_{mb} and ~0.70–0.82 at U_{mf}, a bit less than for the higher columns used in flow experiments (see Figure 6). The duration of complete defluidization of the static columns is close to that of the flow and, as expected, increases with the column height as the pore pressure diffusion timescale is proportional to H^2/D. Note that in the case of initially expanded columns fluidized at U_{mb}, the rate of pressure decrease depends both on pressure diffusion and on bed contraction related to particle settling. As a consequence, for a given column height, P/P_L at a given time as well as the duration of defluidization are larger in columns initially fluidized at U_{mb} than in those fluidized at U_{mf}. Considering a column and flow height of 6 cm, we highlight that at a given time P/P_L in the flow during its constant velocity and stopping phases is higher than in the static column, and it is even up to about twice that in the column in case of initial fluidization at U_{mb}.

4. Discussion

4.1. Origins of the Pressure Signals

4.1.1. Causes of Underpressure at the Flow Head

[22] We now discuss the possible mechanisms that are likely to explain the characteristics of the pressure signals measured in the experiments, and these are summarized in Figure 10. We first address the origin of the underpressure (i.e., pressure less than atmospheric) in the channel, measured as soon as the flow front arrives at the sensors. Underpressure relative to the ambient at the flow head has already been measured in experimental debris flows [*Iverson*, 1997], and in air-particle mixtures including natural snow avalanches [*McElwaine and Turnbull*, 2005] as well as experimental flows such as large-scale ping-pong ball avalanches [*McElwaine and Nishimura*, 2001] and small-scale laboratory gravity currents on steep slopes [*Turnbull and McElwaine*, 2008, 2010].

[23] *McElwaine* [2005] developed a model, based on Bernoulli's theorem, for an inviscid gravity current down an incline. The model gives solution for the fluid pressure along the substrate, ahead of the current front and at the base of the current head [see *McElwaine*, 2005, Figure 3]. First, ambient air pressure is positive ahead of the current and increases to a maximum equal to $\rho_a u^2/2$ at the front, where ρ_a is the air density and u is the air velocity assumed to be equal to that of the front. In our experiments, this positive pressure was of the order of 1 Pa, and could not be detected with the sensors used. Second, air pressure at the base of the current head decreases with distance behind the front and may become negative, so that

$$P = \frac{1}{2}\rho_a u^2\left(1 - \frac{\kappa r}{R}\right) + 2g(\rho - \rho_a) r \sin\left(\frac{\phi}{2}\right)\cos\left(\theta + \frac{\phi}{2}\right), \quad (7)$$

where R is the effective length of the current (aerodynamic flow radius), $r = (t_0 - t)U$ is the distance from the front where t_0 is the moment the front arrives at the sensor and U is the flow velocity, g is gravity acceleration, ρ is the (bulk) flow density, ϕ is the front angle with the substratum, θ is the slope of the incline, and κ is a constant ≈1.01. Behind the effective length, it is assumed that the pressure returns to

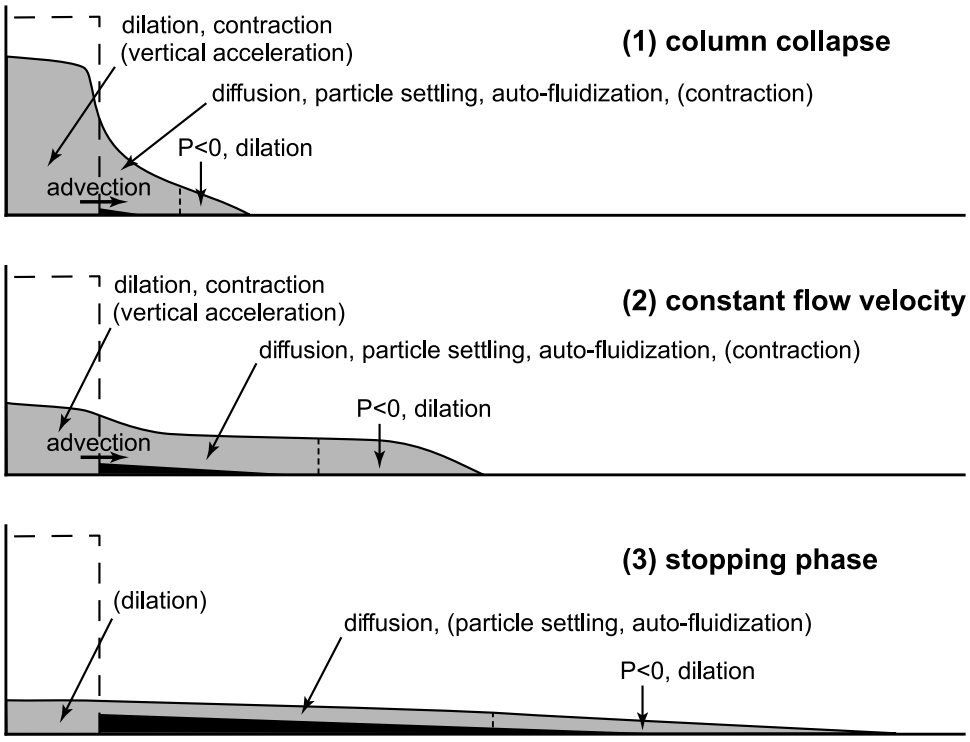

Figure 10. Mechanisms accounting for the pore pressure measured in initially fluidized flows, with second order processes in brackets. The small vertical dashed line separates the zones of underpressure at the flow head, where $P < 0$ denotes the mechanism proposed by *McElwaine* [2005] (see text for details), and of overpressure in the body whose basal deposit is shown (black). The processes acting in initially dry flows are auto-fluidization and $P < 0$.

zero. In our case, $\theta = 0$ and the first term in equation (7) is negligible for R being of the order of the flow height, so that equation (7) becomes

$$P \approx g(\rho - \rho_a)(t_0 - t)U \sin(\phi). \quad (8)$$

Note that $t_0 - t < 0$, and that P has the same dimension as $(\rho - \rho_a)U^2$.

[24] Figure 11 shows the underpressure measured during the constant velocity phase of our experimental flows. As mentioned already, the minimum pressure $P_{\min}$ is approximately constant during that phase. In detail, however, $P_{\min}$ in initially fluidized flows slightly decreases (at U_{mb}) or increases (at U_{mf}) when the distance increases. In order to match $P_{\min}$ in the experiments, we calculated the theoretical pressure with equation (8), from t_0 (at $P = 0$) to the time of $P_{\min}$, so that the parameters to be fitted were the flow density (ρ) and the flow velocity (U). There are, however, limitations regarding the applicability of the model to our experiments. The structure of the experimental flows close to the front could be different from that assumed in the model. The value of $P_{\min}$ was fitted at a distance r larger than the effective length, so that calculation was strictly valid only at early stages of underpressure. Furthermore, we also addressed the initially dry flows though the model does not strictly apply to them. Note that underpressure may also result from other processes, as discussed at the end of this section as well as in section 4.1.3.

[25] We calculated the flow parameters required to fit $P_{\min}$ with equation (8) by considering the front angles observed in our experiments, which decreased with the distance travelled (Figure 3, Table 1). Firstly, we assumed that U in equation (8) was equal to U_f observed in experiments, and obtained bulk flow density values much less than ρ_b~1450 kg m^{-3} (Table 1). This implies very high degrees of homogeneous expansion of the mixtures of at least ~70–200% (initially fluidized flows) and ~220–280% (dry flows), which is evidently not true from observation of the videos. Secondly, we calculated U required to fit $P_{\min}$ assuming that the flow density was equal to that of the initial mixture ρ_b (ρ = 1450 kg m^{-3}) (Table 1). In that case, values of U are smaller than U_f. Interestingly, U is about one third to one half U_f, as shown also in Figure 4 for the middle part of the sliding head, approximately where $P_{\min}$ is generated. We point out that the normalized pressure $-P_{\min}/\rho U^2$ is then about two times smaller in dry flows than in initially fluidized ones (Table 1). All else being equal, this might reflect contrasting degrees of fluidization of the head of both types of flows, and in turn implies that the head of the initially fluidized flows remained at least partially fluidized. In summary, bearing in mind the limitations of applicability of the model to our experiments, the above analysis suggests that the sliding head of the flows had a particle concentration close to that of the initial mixture and generated underpressure according to *McElwaine*'s [2005] model, as long as we accept the required values for the flow velocity U at the base of the sliding head. There are uncertainties regarding

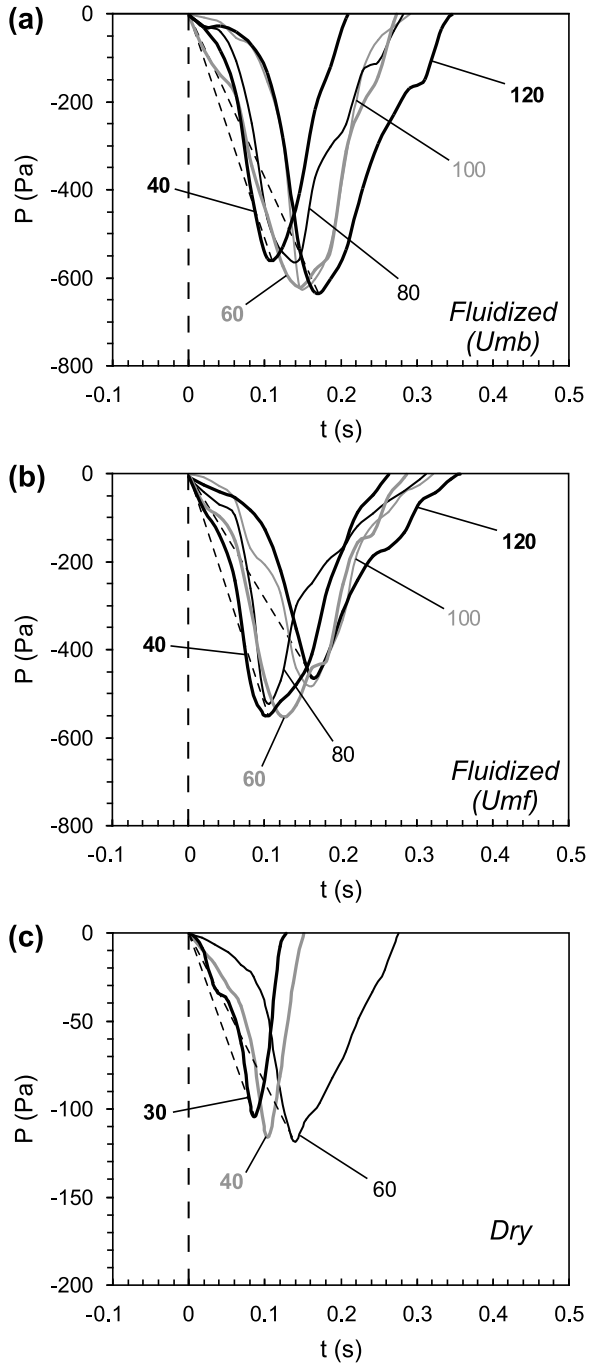

Figure 11. Underpressure measured in the channel during the constant velocity phase of flows initially fluidized at (a) U_{mb} or (b) U_{mf}, and of (c) dry flows. The data are from Figure 6. Pressure (P) is shown as a function of time (t), and $t = 0$ indicates arrival of the flow front at the sensors. Indices denote the distance (in cm) of the sensors from the reservoir gate. The thin dashed lines are the model from equation (8) that fit P_{min}, for the most proximal and distal sensors considered. See text for details.

the degree of fluidization of the head during the constant front velocity phase, but this remained probably close to that of the initial column before release. Though the amount of underpressure appeared to be controlled by this degree of fluidization, it depended primarily on the basal flow velocity. In this context, the decrease of P_{min} while the flow front velocity was constant during the early collapse phase of the initially fluidized flows at $h_0 = 40$ cm (Figure 6) may reflect an increasing basal velocity. Note also that sliding of the granular material above the nose of the basal deposit may also explain (1) the second underpressure stage measured in the body of the dry flows at the entrance of the channel and (2) why the underpressure zone in the initially fluidized flows extends behind the tip of the deposit at late stages of emplacement.

[26] Underpressure at the flow head could be generated by other mechanisms. It could result from the presence of a boundary layer at the base of the flows that we could not detect. Dilation at the flow head with particles and interstitial air moving relatively upwards and downwards, respectively, thus generating drag, could be another mechanism to generate underpressure. However, assuming this is the only active process, this would correspond to a rather complex structure of the flow head. Dilation would increase from the front, would be maximum about where P_{min} is generated, and then would decrease behind. By simply assuming that the dilating mixture behaves similarly to a fluidized bed, for which the pore fluid pressure varies linearly with the interstitial air velocity, then the maximum air-particle relative velocity is $U_r = (P_{min}U_{mf})/P$, where P is the pore pressure in a bed of given height h fluidized at U_{mf}. Taking into account the flow height and P_{min} measured in the experiments, then U_r (at P_{min}) is ~0.4–0.6 cm s^{-1} and ~0.1–0.2 cm s^{-1} in initially fluidized and dry flows, respectively, which appear as possible values according to the flow dimensions and velocities. Dilation could act along with sliding as described in the previous paragraph, and U_r would then be smaller than indicated just above. The effects of dilation of the mixture without differential motion between the solid and fluid phases are considered in section 4.1.3.

4.1.2. Causes of Overpressure in the Flow Body

[27] The positive pressure (i.e., more than atmospheric) measured in the body of the initially fluidized flows, without any air supply from the substrate, primarily derives from advection of the initial pore pressure generated in the reservoir. In the channel, the decrease of P_{max} as the distance from the reservoir increases and of the pore pressure with time after P_{max} at a given location both suggest that pore pressure diffusion is a fundamental process until the flows are completely defluidized and stop. Diffusion is relatively

Table 1. Characteristics of the Flows and Values of the Bulk Flow Density ρ and Flow Velocity U Required to Fit P_{min} Using Equation (8)[a]

	Initial Condition					
	Umb		Umf		Dry	
	SL 40 cm	SL 120 cm	SL 40 cm	SL 120 cm	SL 30 cm	SL 60 cm
ϕ (deg)	25	10	25	10	12	7
ρ[b] (kg m^{-3})	490	868	562	744	380	453
U[c] (cm s^{-1})	90	153	88	116	42	63
U/U_f [c]	0.35	0.60	0.39	0.51	0.26	0.39
$-P_{min}/\rho U^{2}$[c]	0.06	0.07	0.06	0.07	0.03	0.03

[a]SL, sensor location.
[b]$U = U_f$.
[c]Density ρ = 1450 kg m^{-3}.

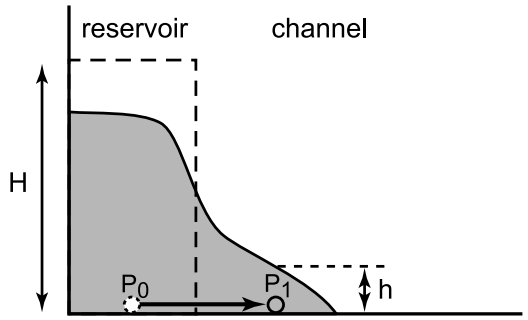

Figure 12. Advection of the pore fluid pressure from the reservoir to the channel (horizontal arrow). The pressure in the initially fluidized column is $P_0 = \rho_b g H$. If the timescale of pressure diffusion is large compared with that of advection, then pressure in the flow can be more than lithostatic as $P_1 \sim \rho_b g H > \rho_b g h$.

slow compared with advection, because at the entrance of the channel pore pressure in the flows generated from the base of the thicker fluidized columns remains close to that in the reservoir (Figure 6) and is then larger than lithostatic (Figure 12). Note that pressure in the reservoir can be larger than lithostatic, and this is discussed in section 4.1.3. In slightly expanded mixtures, settling of the particles also acts opposite to pressure diffusion because it generates pore pressure and hence increases the defluidization timescale, as mentioned earlier for static columns (Figure 9). This occurs readily in flows initially fluidized at U_{mb}, but may happen as well in other types of flows provided they experience sufficient expansion during emplacement. Particle settling might generate overpressure in dry flows, but these, however, are initially not expanded and can only experience Reynolds dilation.

[28] Overpressure in the initially dry flows is an important observation. This suggests that viscous drag is induced by differential motion between the unsteady particles and the interstitial air during bulk movement of the mixture. This dynamic, motion-induced pore pressure arises at early stages as the flowing granular material is sheared. It is more important in the reservoir and at the entrance of the channel, where at least up to ~16% of the weight of the particles is supported, and is smaller further away probably because of less efficient air-particle interactions. We point out that a dimensional analysis of experiments similar to those presented in this paper showed that strong viscous air-particle interactions can develop in these internally sheared flows, thus promoting at least partial support of the weight of the particles [*Roche et al.*, 2008]. This phenomenon will be referred to auto-fluidization hereafter for convenience though we acknowledge that full bed support is not achieved. We highlight that auto-fluidization of our air-particle flows has an internal origin and does not require any external fluidizing gas. This is similar to the model of *Huang et al.* [2009] for granular flows sheared in rotating drums and that can be fluidized by internal cycling air. In contrast, this differs from the conclusion of *Bareschino et al.* [2008] for flows in rotating drums invoking air ingestion at the front through plunging avalanches. Note that auto-fluidization is likely to occur in initially fluidized flows as well, at an amount at least equivalent to that in dry flows, and this would contribute to generate high pore fluid pressure along with the other mechanisms described in this paper. This may explain why the pore pressure in the flows is larger than in defluidizing static columns of equivalent height at given time (Figure 9), though comparison between the dynamic and static cases is not straightforward as discussed in section 3.4.

4.1.3. Voidage Variation of the Fluidized Air-Particle Mixture

[29] We now consider the influence of dilation and contraction of the air-particle mixture on the pore fluid pressure. The following better applies to fluidized mixtures, i.e., for which stresses are readily transmitted by the fluid phase. The perfect gas law indicates that PV/T is constant for a constant mass of gas, where P, V, and T are the pressure, volume, and temperature of air, respectively. Assuming that T is constant, then

$$P_2 = P_1 \frac{V_1}{V_2}, \tag{9}$$

where indices denote two successive stages. We note from equation (9) that 1% dilation (contraction) of a fluidized air-particle mixture at pressure about equal to that of the ambient atmosphere, so that $P_1 \sim 10^5$ Pa, causes a pressure decrease (increase) of ~1000 Pa. In case of dilation of the mixture, the internal air pressure decreases as the ambient cannot supply sufficient new air to compensate the pressure drop inside the flow. Variation of the voidage of the air-particle mixture may occur both in the reservoir once the column is released and in the subsequent flows.

[30] In the flows, dilation could generate underpressure at the flow head, and $P_{\min}$ measured would correspond (assuming pressure decrease from $P = 0$) to a dilation of ~0.5–0.6% and ~0.1% in initially fluidized and dry flows, respectively. Note that the second underpressure stage measured in dry flows would be compatible with an equivalent amount of dilation of the granular material flowing above the nose of the basal deposit. In case underpressure at the head would also be generated by the process proposed by *McElwaine* [2005] (section 4.1.1), then the amount of dilation would be smaller than indicated above. Generation of underpressure through dilation, however, would require a rather complex structure of the flow head in terms of degree of dilation, as mentioned in section 4.1.1. Furthermore, we highlight that underpressure measured at the head of debris flows [e.g., *Iverson*, 1997] appears to be incompatible with the low compressibility of the interstitial water if one assumes a pressure decrease through dilation.

[31] Pressure variations measured at the base of the fluidized columns in the reservoir can be explained by successive dilation and contraction stages of the air-particle mixture (Figure 10). Once the column is released, dilation may occur readily as the mixture stretches when the flow enters the channel and/or as pressure at the base of the column tend to equilibrate with the lower atmospheric pressure. In this context, the sudden pressure decrease of ~4500 Pa right after gate opening in columns fluidized at U_{mb} and U_{mf} (Figure 6) indicates dilation of ~4.5%, so that the total expansion at U_{mb} relative to the initial loosely packed state is ~7.5–8.5%. Then, the following pressure increase up to values that can be larger than lithostatic at the

end of the collapse phase may be generated by two means: (1) the acceleration of the falling particles within the reservoir, and (2) a contraction of the mixture, and successive transient stages of slight dilation and contraction would account for the pressure oscillations observed. In case (1), as the gate is open and the whole granular mass falls under the influence of gravity, then the basal pore pressure counterbalances the weight of the particles (as before release) plus the force related to their acceleration. The excess pore pressure generated is then $P_e = \rho U_c^2$, where U_c is the vertical velocity of the collapsing column ~80–85 cm s^{-1}, so that P_e~1000 Pa. This, however, is insufficient to account for the pressure measured at the end of the collapse phase. In case (2), at both U_{mb} and U_{mf}, P-P_L is ~1500 Pa (as P/P_L~1.5) at the end of the collapse phase when the reservoir is about half emptied. Taking into account the possible excess pressure of ~1000 Pa caused by vertical motion of the mixture, the difference of ~500 Pa indicates a contraction of ~0.5% compared to the initial static fluidized state before release (in case no excess pore pressure would be generated by column collapse, then contraction would be only ~1% more). This means that the packing at U_{mf} is then slightly larger than the loose packing of the initial column, which is plausible as loose granular beds can compact by a few percents when subjected to external forcing [*Duran*, 1999]. In contrast, beds fluidized at U_{mb} are still slightly expanded, at an amount of ~2.5–3.5%. In summary, to explain the pressure increase following the initial decrease in the reservoir during the column collapse phase, we favor contraction of the air-particle mixture possibly combined with its vertical acceleration. Interestingly, at both U_{mb} and U_{mf}, slight dilation related to the sudden acceleration of the flows when they enter the second, constant flow velocity phase can explain why P/P_L slightly decreases at that stage. Then, at U_{mb}, contraction of the mixture as the granular column terminates to collapse can account for the slight increase of P/P_L during that constant velocity phase, and pressure returns to lithostatic as the mixtures reacquires its initial voidage during the last, stopping phase. Note that this effect is less pronounced in columns fluidized at U_{mf}, for which contraction is more difficult to achieve because of their initial non-expanded state.

[32] In the case of the initially dry flows, the sudden pressure increase of ~800 Pa in the reservoir right after gate opening could suggest a contraction of ~0.8%. However, as the granular column is initially not fluidized nor expanded, a pressure increase through voidage reduction is probably difficult to achieve. Furthermore, the mixture is rather expected to dilate once in motion. In consequence, auto-fluidization as described in the previous section better explains the positive pressure generated. Nevertheless, voidage variation could cause the small pressure fluctuations measured once the granular material is partially fluidized during flow emplacement.

4.2. Implications for Geophysical Flows

[33] Our experimental study applies to dense (or the dense part of) subaerial geophysical flows propagating on a subhorizontal slope, and particularly to cases where fluid-particle interactions at initial stages are strong enough to generate a fluidized mixture with high pore fluid pressure. The experiments are relevant to flows rich in fine particles, which, regarding the type of air fluidization processes, belong to the *Geldart* [1973] group A. In the volcanological context, these conditions are readily achieved in ash-rich pyroclastic flows as a fluidized mixture of gas and particles is emitted at the eruptive vent. The flows then basically defluidize as they propagate, though local and transient gas supply may be provided from either internal or external sources. Note that particle aggregation and temperature-derived buoyancy were negligible in the experiments, unlike to what it may happen for pyroclastic flows in nature. These experiments may also apply to other types of flows such as dense snow avalanches [*Bartelt et al.*, 1999], as these may be fluidized by air entrainment at the front as the air-snow mixture is relatively dilute during initial acceleration on steep slopes [*Rastello and Hopfinger*, 2004; *Turnbull and McElwaine*, 2007]. Uncertainties, however, concern the type of air fluidization processes of snow particles, and aggregation of these particles then forming a coherent plug may complicate this simple picture [*Salm*, 1993]. The pore fluid pressure and internal kinematic data reported in this study give insights into the structure of these geophysical flows. These may consist of a (at least) partially fluidized sliding head generating underpressure, followed by an almost fully fluidized body at the base of which a deposit forms and aggrades upwards at a nearly constant rate, and both the head and body are sheared pervasively (Figure 13). As the flow basically defluidizes during transport, the degree of fluidization at a given time is expected to decrease from the source, provided auto-fluidization is not efficient enough.

[34] Regarding pyroclastic flows, the experimental results are consistent with several field observations. Sliding and associated shear at the base of the flow head may generate erosion features, as discussed also by *Girolami et al.* [2010]. This is likely to occur if large lithic clasts segregate in the lowermost part of the flow [*Druitt and Sparks*, 1982; *Sparks et al.*, 1997; *Pittari and Cas*, 2004] and are dragged by the (partially) fluidized ash matrix [*Dufek and Bergantz*, 2007a, 2007b; *Dufek et al.*, 2009; *Roche et al.*, 2005], or when the flow has acquired a frictional behavior once defluidized at late stages. In case of a substrate consisting of an unconsolidated loose granular material, underpressure relative to the ambient atmosphere at the base of the head may cause an upward-directed pressure gradient, provided atmospheric pressure is maintained in the pores of the substrate as the latter is overlain by the flow (Figure 13). This, along with basal shear (if strong enough), may act as an efficient mechanism to entrain loose material from the ground. Substrate-derived clasts are often encountered in pyroclastic flow deposits and may be the witness of such a process. For example, slabs of pumice fall deposits a few tens of centimeters-thick can be incorporated into overlying pyroclastic flow deposits [*Druitt and Sparks*, 1982, Figure 8]. More generally, accidental substrate-derived clasts could be incorporated into the flow head, possibly contributing to form the (ground) layer 1 observed in many deposits [*Wilson*, 1986]. The mechanism for clasts incorporation we discuss here is an alternative to the proposed turbulent boundary layer at the flow base induced by surface roughness of the substrate [*Buesch*, 1992] or to the sudden flow acceleration on local steep slope [*Suzuki-Kamata*, 1988]. As experiments showed that the rear limit of the underpressure

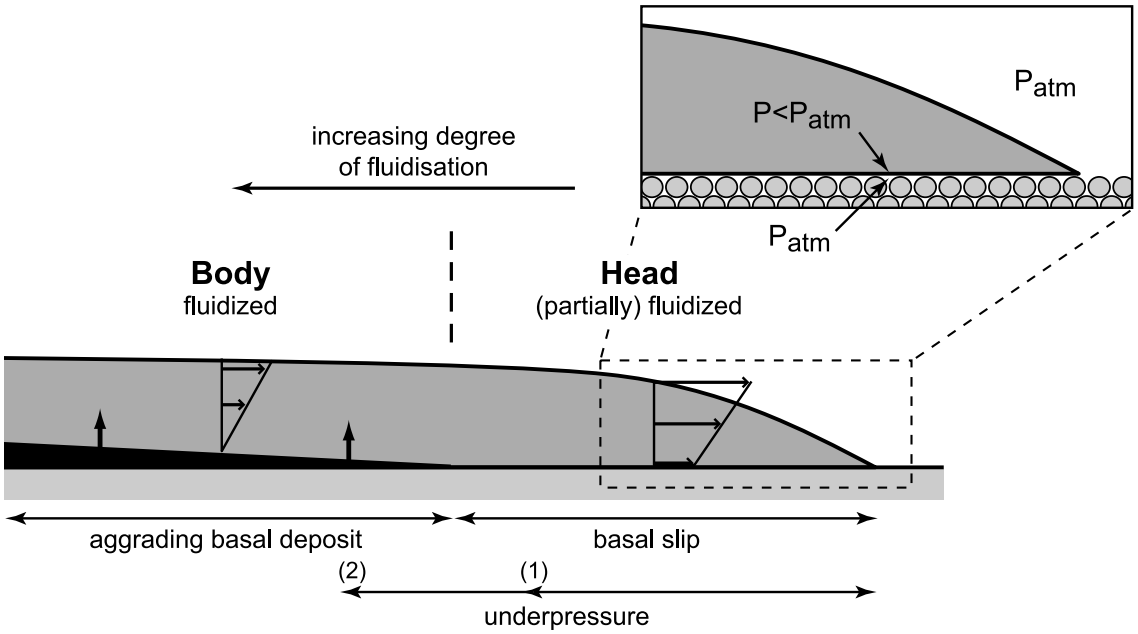

Figure 13. Structure of a geophysical flow inferred from the present study. Horizontal and vertical arrows in the flow head and body indicate the internal velocity and aggradation of the basal deposit (black), respectively. Numbers denote the shift of the rear limit of the underpressure zone at early (1) and late (2) stages. In the latter case, this zone extends towards the distal part of the deposit. The close-up is the sketch of the head passing over a substrate consisting of an unconsolidated granular material (circles), not to scale. Pressure in the pores of the substrate is that of the ambient atmosphere (P_{atm}), and underpressure ($P < P_{atm}$) at the base of the sliding head generates an upward-directed pressure gradient.

zone migrated to the basal deposit at late stages of emplacement, particles deposited from the flow body might be reworked if a sufficient pressure gradient developed. Neglecting this process, the data of *Girolami et al*. [2010] as well as those reported in the present study suggest that the basal deposit in the body may aggrade at a nearly constant rate until the overlying flow is entirely consumed, as also inferred from textural studies of pyroclastic flow deposits [*Branney and Kokelaar*, 1992, 2002]. The body of pyroclastic flows is likely to be almost fully fluidized provided pore pressure diffusion is relatively slow and viscous gas-particle interactions caused by differential motion between the solid and fluid phases are strong enough, the latter occurring through mixture contraction and particle settling as well as auto-fluidization as defined above. Internal inter-particle contact stresses may then be considerably reduced, thus conferring an inertial fluid-like behavior despite the very high particle concentration [e.g., *Roche et al.*, 2008] and the presence of a sliding head. In this context, the contribution of the head to the whole flow resistance would be negligible, though basal shear might contribute to generate erosion features as described above. At late stages of emplacement, particle interactions are expected to become dominant once pore pressure has decreased sufficiently, thus promoting a transition from a fluid-inertial to a granular-frictional behavior [*Roche et al.*, 2008].

[35] The relative magnitudes of the pore pressure diffusion and advection timescales are important regarding the flow dynamics. Close to the source, the pore pressure can be larger than lithostatic if diffusion is relatively slow and the flow thins rapidly (i.e., Figure 12). The issue of the flow run out can be addressed considering the dimensionless pore pressure number defined by *Iverson and Denlinger* [2001]. This number (N_p) represents the ratio of the timescale for flow run out related to pressure advection, $(L/g)^{1/2}$, to the timescale for pressure diffusion, h^2/D, so that

$$N_p = \frac{D(L/g)^{1/2}}{h^2}. \tag{10}$$

In our experiments, with D~0.01 m^2 s^{-1} [*Montserrat et al.*, 2007] and h~0.06 m, then N_p~1. This is larger but close to that for pyroclastic flows as N_p~0.1 if one assumes a same value of D, L~1000 m, and h~1 m. Note, however, that likely smaller hydraulic diffusivity and larger flow thickness values in natural flows would decrease the pore pressure number, thus indicating that high pore fluid pressure would persist relatively longer than in experiments. In consequence, assuming that the mechanisms of pore pressure generation are of comparable relative magnitude at the natural and laboratory scales, the flow run out in nature would be relatively larger than in the experiments. Nevertheless, the structure of the natural flows is expected to be similar to that of their experimental analogs, though more elongated horizontally.

5. Conclusion

[36] The emplacement dynamics of dense air-particle gravitational flows were investigated through analogue laboratory experiments. We carried out measurements of the pore fluid pressure in dam break flows generated from the

release of fluidized and nonfluidized granular columns. The internal structure of the flows was also investigated from analyses of high-speed videos. The experimental setup was designed to allow for noninvasive measurement of the pore pressure relative to that of the ambient atmosphere, and we studied how it varied both spatially and temporarily during flow emplacement. All types of flows consisted of (1) a sliding head that caused relative underpressure, followed by (2) a body that generated relative overpressure and at the base of which a deposit aggraded at a nearly constant rate. Both the head and body were sheared pervasively. The measured pressure signal resulted from the combination of several processes (Figure 10). The underpressure generated by the sliding head may be explained by two mechanisms, possibly acting together. Dilation of the flow head of the order of 0.1–1% may generate the amount of the peak of underpressure (P_{min}) observed. Underpressure was also accounted for by the theory developed by *McElwaine* [2005] assuming an inviscid fluid flow, though uncertainties remain on the applicability of the model to our experimental flows. P_{min} was primarily proportional to the basal flow velocity, but depended also on the degree of fluidization of the head as it was relatively smaller in dry flows than in initially fluidized ones whose head was probably at least partially fluidized. We acknowledge, however, that this latter issue deserves further investigation. For initially fluidized mixtures, overpressure in the flow body primarily derived from advection of the pore pressure generated in the initial column, and the flows defluidized by pressure diffusion until they came to halt. The amount of overpressure depended on the relative timescales of pressure advection and diffusion, on auto-fluidization processes, and on variation of the voidage of the air-particle mixture. At early stages, relatively slow pressure diffusion led the pore pressure in the thin flows to be larger than lithostatic. Auto-fluidization was evidenced in initially dry flows, for which at least up to ~16% of the weight of the particles was supported. It arose from shear-induced, relative motion between the particles and the interstitial air. Auto-fluidization occurred probably also in initially fluidized flows and then contributed to generate positive pore pressure along with the other processes. Additionally, slight dilation or contraction of the flow body with air drag and/or pore volume variation led the pore pressure to transiently decrease or increase, respectively. We highlight that, in the case of initially slightly expanded (~3–4%) fluidized mixtures, high pore fluid pressure persisted for most the flow propagation as (at least) ~70 to 100% of the weight of the particles was supported, thus showing that particle-particle shear interactions were then very much reduced. This provides an explanation for the inertial fluid-like behavior of these flows until the beginning of their stopping phase [*Roche et al.*, 2008].

[37] Our study better applies to pyroclastic flows propagating on subhorizontal slopes, but it may also have interest for other types of dense two-phase gravity currents such as snow avalanches. It shows that accurately modeling gas-particle flows requires taking into account detailed processes of fluid-solid interactions whose degree depend on variation of the voidage of the mixture and on the relative velocity of the two phases [e.g., *Meruane et al.*, 2010]. Pyroclastic flows may consist of two distinct parts, both sheared pervasively: (1) a (at least) partially fluidized sliding head that may erode the substrate and where incorporation of accidental lithic clasts can occur; and (2) a fluidized body at the base of which a deposit aggrades [e.g., *Branney and Kokelaar*, 1992, 2002] at a nearly constant rate. Even though these flows are highly concentrated and have a sliding head, they are expected to propagate as inertial fluids for most their emplacement, thus being highly mobile [e.g., *Roche et al.*, 2008]. Particle-particle shear interactions may dominate the flow dynamics only at late stages, when the pore fluid pressure has sufficiently decreased by diffusion and other processes that are likely to increase the pore pressure have become no longer efficient enough.

[38] **Acknowledgments.** This work would not have been possible without the technical assistance of Delphine Auclair, Eric Brut, Jean-Louis Fruquière, and Jean-Luc Piro at Laboratoire Magmas et Volcans. Thanks also to Frédéric Chausse (Lasmea, U. Blaise Pascal) for his advice on the experimental setup. This work was supported by Institut de Recherche pour le Développement (IRD, France), and ANR VolBiFlo (France) and ECOS-Conicyt C06U01 (France-Chile) projects. An earlier version benefited from stimulating discussions with Tim Druitt, David Jessop, and Jim McElwaine. We thank the anonymous Associate Editor and reviewers for their constructive comments.

References

Bareschino, P., A. Marzocchella, P. Salatino, L. Lirer, and P. Petrosino (2008), Self-fluidization of subaerial rapid granular flows, *Powder Technol.*, *182*, 323–333, doi:10.1016/j.powtec.2007.12.010.

Bartelt, P., B. Salm, and U. Gruber (1999), Calculating dense snow avalanche runout using a Voellmy-fluid model with active/passive longitudinal straining, *J. Glaciol.*, *45*, 242–254.

Berti, M., and A. Simoni (2005), Experimental evidences and numerical modelling of debris flow initiated by channel runoff, *Landslides*, *2*, 171–182, doi:10.1007/s10346-005-0062-4.

Branney, M. J., and P. Kokelaar (1992), A reappraisal of ignimbrite emplacement: Progressive aggradation and changes from particulate to non-particulate flow during emplacement of high-grade ignimbrite, *Bull. Volcanol.*, *54*, 504–520, doi:10.1007/BF00301396.

Branney, M. J., and B. P. Kokelaar (2002), Pyroclastic Density Currents and the Sedimentation of Ignimbrites, *Geol. Soc. Mem.*, vol. 27, 152 pp., Geol. Soc., London.

Buesch, D. C. (1992), Incorporation and redistribution of locally derived lithic fragments within a pyroclastic flow, *Geol. Soc. Am. Bull.*, *104*, 1193–1207, doi:10.1130/0016-7606(1992)104<1193:IAROLD>2.3.CO;2.

Cassar, C., M. Nicolas, and O. Pouliquen (2005), Submarine granular flows down inclined planes, *Phys. Fluids*, *17*, 103301, doi:10.1063/1.2069864.

Druitt, T. H. (1998), Pyroclastic density currents, in *The Physics of Explosive Volcanic Eruptions*, edited by J. S. Gilbert and R. S. J. Sparks, *Geol. Soc. Spec. Publ.*, *145*, 145–182.

Druitt, T. H., and R. S. J. Sparks (1982), A proximal ignimbrite breccias facies on Santorini, Greece, *J. Volcanol. Geotherm. Res.*, *13*, 147–171, doi:10.1016/0377-0273(82)90025-7.

Druitt, T. H., G. Avard, G. Bruni, P. Lettieri, and F. Maez (2007), Gas retention in fine-grained pyroclastic flow materials at high temperatures, *Bull. Volcanol.*, *69*, 881–901, doi:10.1007/s00445-007-0116-7.

Dufek, J., and G. W. Bergantz (2007a), Dynamics and deposits generated by the Kos Plateau Tuff eruption: Controls of basal particle loss on pyroclastic flow transport, *Geochem. Geophys. Geosyst.*, *8*, Q12007, doi:10.1029/2007GC001741.

Dufek, J., and G. W. Bergantz (2007b), Suspended load and bed-load transport of particle-laden gravity currents: The role of particle-bed interaction, *Theor. Comput. Fluid Dyn.*, *21*, 119–145, doi:10.1007/s00162-007-0041-6.

Dufek, J., J. Wexler, and M. Manga (2009), Transport capacity of pyroclastic density currents: Experiments and models of substrate-flow interaction, *J. Geophys. Res.*, *114*, B11203, doi:10.1029/2008JB006216.

Duran, J. (1999), *Sands, Powders and Grains: An Introduction to the Physics of Granular Materials*, Springer-Verlag, New York.

Freundt, A., and M. Bursik (1998), Pyroclastic flow transport mechanisms, in *From Magma to Tephra, Modelling Physical Processes of Explosive Volcanic Eruptions*, edited by A. Freundt and M. Rosi, pp. 173–245, Elsevier, New York.

Gabet, E., and S. M. Mudd (2006), The mobilization of debris flows from shallow landslides, *Geomorphology*, *74*, 207–218, doi:10.1016/j.geomorph.2005.08.013.

Geldart, D. (1973), Types of gas fluidization, *Powder Technol.*, *7*, 285–292, doi:10.1016/0032-5910(73)80037-3.

Geldart, D., and A. C. Y. Wong (1985), Fluidization of powders showing degrees of cohesiveness—II. Experiments on rates of deaeration, *Chem. Eng. Sci.*, *40*, 653–661, doi:10.1016/0009-2509(85)80011-7.

Gilbertson, M. A., D. E. Jessop, and A. J. Hogg (2008), The effects of gas flow on granular currents, *Philos. Trans. R. Soc. Ser. A*, *366*, 2191–2203, doi:10.1098/rsta.2007.0021.

Girolami, L., O. Roche, T. H. Druitt, and T. Corpetti (2010), Particle velocity fields and depositional processes in laboratory ash flows, with implications for the sedimentation of dense pyroclastic flows, *Bull. Volcanol.*, *72*(6), 747–759, doi:10.1007/s00445-010-0356-9.

Hopfinger, E. J. (1983), Snow avalanche motion and related phenomena, *Annu. Rev. Fluid Mech.*, *15*, 47–76, doi:10.1146/annurev.fl.15.010183.000403.

Huang, Q., H. Zhang, and J. Zhu (2009), Experimental study on fluidization of fine powders in rotating drums with various wall friction and baffled rotating drums, *Chem. Eng. Sci.*, *64*, 2234–2244, doi:10.1016/j.ces.2009.01.047.

Hutchinson, J. N. (1986), A sliding-consolidation model for flow slides, *Can. Geotech. J.*, *23*, 115–126, doi:10.1139/t86-021.

Ilstad, T., J. G. Marr, A. Elverhøi, and C. A. Harbitz (2004), Laboratory studies of subaqueous debris flows by measurements of pore-fluid pressure and total stress, *Mar. Geol.*, *213*, 403–414, doi:10.1016/j.margeo.2004.10.016.

Iverson, R. M. (1997), The physics of debris flows, *Rev. Geophys.*, *35*, 245–296, doi:10.1029/97RG00426.

Iverson, R. M. (2005), Regulation of landslide motion by dilatancy and pore pressure feedback, *J. Geophys. Res.*, *110*, F02015, doi:10.1029/2004JF000268.

Iverson, R. M., and R. P. Denlinger (2001), Flow of variably fluidized granular masses across three-dimensional terrain: 1. Coulomb mixture theory, *J. Geophys. Res.*, *106*, 537–552, doi:10.1029/2000JB900329.

Iverson, R. M., M. E. Reid, and R. G. LaHusen (1997), Debris-flow mobilization from landslides, *Annu. Rev. Earth Planet. Sci.*, *25*, 85–138, doi:10.1146/annurev.earth.25.1.85.

Iverson, R. M., M. E. Reid, N. R. Iverson, R. G. LaHusen, M. Logan, J. E. Mann, and D. L. Brien (2000), Acute sensitivity of landslide rates to initial soil porosity, *Science*, *290*, 513–516, doi:10.1126/science.290.5491.513.

Major, J. J. (2000), Gravity-driven consolidation of granular slurries: Implications for debris-flow deposition and deposit characteristics, *J. Sediment. Res.*, *70*, 64–83, doi:10.1306/2DC408FF-0E47-11D7-8643000102C1865D.

Major, J. J., and R. M. Iverson (1999), Debris-flow deposition: effects of pore-fluid pressure and friction concentrated at flow margins, *Geol. Soc. Am. Bull.*, *111*, 1424–1434, doi:10.1130/0016-7606(1999)111<1424:DFDEOP>2.3.CO;2.

McArdell, B. W., P. Bartelt, and J. Kowalski (2007), Field observations of basal forces and fluid pore pressure in a debris flow, *Geophys. Res. Lett.*, *34*, L07406, doi:10.1029/2006GL029183.

McElwaine, J. N. (2005), Rotational flow in gravity current heads, *Philos. Trans. R. Soc. Ser. A*, *363*, 1603–1623, doi:10.1098/rsta.2005.1597.

McElwaine, J. N., and K. Nishimura (2001), Ping-pong ball avalanche experiments, *Spec. Publ. Int. Assoc. Sedimentol.*, *31*, 135–148.

McElwaine, J. N., and B. Turnbull (2005), Air pressure data from the Vallée de la Sionne avalanches of 2004, *J. Geophys. Res.*, *110*, F03010, doi:10.1029/2004JF000237.

Meruane, C., A. Tamburrino, and O. Roche (2010), On the role of the ambient fluid on gravitational granular flow dynamics, *J. Fluid Mech.*, *648*, 381–404, doi:10.1017/S0022112009993181.

Montgomery, D. R., K. M. Schmidt, W. E. Dietrich, and J. McKean (2009), Instrumental record of debris flow initiation during natural rainfall: Implications for modeling slope stability, *J. Geophys. Res.*, *114*, F01031, doi:10.1029/2008JF001078.

Montserrat, S., A. Tamburrino, Y. Niño, and O. Roche (2007), Kinematics and pore pressure dynamics in aerated granular flows, paper presented at 32nd Congress of International Association of Hydraulic Engineering and Research, Venice, Italy.

Nishimura, K., F. Sandersen, K. Kristensen, and K. Lied (1995), Measurements of powder snow avalanche, *Surv. Geophys.*, *16*, 649–660, doi:10.1007/BF00665745.

Okada, Y., and H. Ochiai (2008), Flow characteristics of 2-phase granular mass flows from model flume tests, *Eng. Geol.*, *97*, 1–14, doi:10.1016/j.enggeo.2007.10.004.

Okada, Y., K. Sassa, and H. Fukuoka (2004), Excess pore pressure and grain crushing of sands by means of undrained and naturally drained ring-shear tests, *Eng. Geol.*, *75*, 325–343, doi:10.1016/j.enggeo.2004.07.001.

Okura, Y., H. Kitahara, H. Ochiai, T. Sammori, and A. Kawanami (2002), Landslide fluidization process by flume experiments, *Eng. Geol.*, *66*, 65–78.

Pittari, A., and R. A. F. Cas (2004), Sole marks at the base of the late Pleistocene Abrigo Ignimbrite, Tenerife: Implications for transport and depositional processes at the base of pyroclastic flows, *Bull. Volcanol.*, *66*, 356–363, doi:10.1007/s00445-003-0317-7.

Rastello, M., and E. J. Hopfinger (2004), Sediment-entraining suspension clouds: A model of powder-snow avalanches, *J. Fluid Mech.*, *509*, 181–206, doi:10.1017/S0022112004009322.

Rhodes, M. J. (1998), *Introduction to Particle Technology*, John Wiley, Chichester, N. Y.

Roche, O., M. A. Gilbertson, J. C. Phillips, and R. S. J. Sparks (2005), Inviscid behaviour of fines-rich pyroclastic flows inferred from experiments on gas-particle mixtures, *Earth Planet. Sci. Lett.*, *240*, 401–414, doi:10.1016/j.epsl.2005.09.053.

Roche, O., S. Montserrat, Y. Niño, and A. Tamburrino (2008), Experimental observations of water-like behavior of initially fluidized, dam break granular flows and their relevance for the propagation of ash-rich pyroclastic flows, *J. Geophys. Res.*, *113*, B12203, doi:10.1029/2008JB005664.

Salm, B. (1993), Flow, flow transition and runout distances of flowing avalanches, *Ann. Glaciol.*, *18*, 221–226.

Snieder, R., and A. van den Beukel (2004), The liquefaction cycle and the role of drainage in liquefaction, *Granular Matter*, *6*, 1–9, doi:10.1007/s10035-003-0151-9.

Sparks, R. S. J., M. C. Gardeweg, E. S. Calder, and S. J. Matthews (1997), Erosion by pyroclastic flows on Lascar Volcano, *Chile, Bull. Volcanol.*, *58*, 557–565, doi:10.1007/s004450050162.

Suzuki-Kamata, K. (1988), The ground layer of Ata pyroclastic flow deposit, southwestern Japan—Evidence for the capture of lithic fragments, *Bull. Volcanol.*, *50*, 119–129, doi:10.1007/BF01275173.

Turnbull, B., and J. N. McElwaine (2007), A comparison of powder snow avalanches at Vallée de la Sionne with plume theories, *J. Glaciol.*, *53*, 30–40, doi:10.3189/172756507781833938.

Turnbull, B., and J. N. McElwaine (2008), Experiments on the non-Boussinesq flow of self-igniting suspension currents on a steep open slope, *J. Geophys. Res.*, *113*, F01003, doi:10.1029/2007JF000753.

Turnbull, B., and J. N. McElwaine (2010), Potential flow models of suspension current air pressure, *Ann. Glaciol.*, *51*, 113–122, doi:10.3189/172756410791386490.

Wilson, C. J. N. (1986), Pyroclastic flows and ignimbrites, *Sci. Prog. Oxford*, *70*, 171–207.

S. Montserrat, Y. Niño, and A. Tamburrino, Department of Civil Engineering, Universidad de Chile, Casilla 228-3, Santiago, Chile. (smontser@ing.uchile.cl; ynino@ing.uchile.cl; atamburr@ing.uchile.cl)

O. Roche, Clermont Université, Université Blaise Pascal, Laboratoire Magmas et Volcans, BP 10448, F-63000 Clermont-Ferrand, France. (o.roche@opgc.univ-bpclermont.fr)